dehydrogenase by phosphorylation involves no long-range conformational change in the free enzyme. *J. Biol. Chem.* **265,** 3599–3602 (1990).
23. Russo, A. A., Jeffrey, P. D. & Pavletich, N. P. Structural basis of cyclin-dependent kinase activation by phosphorylation. *Nature Struct. Biol.* **3,** 696–700 (1996).
24. Canagarajah, B. J., Khokhlatchev, A., Cobb, M. H. & Goldsmith, E. J. Activation mechanism of the MAP kinase ERK2 by dual phosphorylation. *Cell* **90,** 859–869 (1997).
25. Barford, D., Hu, S. H. & Johnson, L. N. Structural mechanism for glycogen phosphorylase control by phosphorylation and AMP. *J. Mol. Biol.* **218,** 233–260 (1991).
26. Lin, K., Rath, V. L., Dai, S. C., Fletterick, R. J. & Hwang, P. K. A protein phosphorylation switch at the conserved allosteric site in GP. *Science* **273,** 1539–1542 (1996).
27. Altieri, A. S., Hinton, D. P. & Byrd, R. A. Association of biomolecular systems via pulsed field gradient NMR self-diffusion measurements. *J. Am. Chem. Soc.* **117,** 7566–7567 (1995).
28. Güntert, P., Mumenthaler, C. & Wüthrich, K. Torsion angle dynamics for NMR structure calculation with the new program DYANA. *J. Mol. Biol.* **273,** 283–298 (1997).
29. Koradi, R., Billeter, M. & Wüthrich, K. MOLMOL: A program for display and analysis of macromolecular structures. *J. Mol. Graph.* **14,** 51–55 (1996).

Acknowledgements

We thank D. King for analysis by mass spectrometry. This work was supported by the Director, Office of Biological & Environmental Research, Office of Energy Research of the US Department of Energy, and through instrumentation grants from the NSF D.E.W. would also like to thank the Miller Institute for support during part of this work. NMR studies were carried out at the National Magnetic Resonance Facility at Madison with support from the NIH Biomedical Technology Program and additional equipment funding from the University of Wisconsin, NSF Academic Infrastructure Program, NIH Shared Instrumentation Program, NSF Biological Instrumentation Program, and US Department of Agriculture.

Correspondence and requests for materials should be addressed to D.K. (e-mail: dkern@brandeis.edu). Coordinates for the NMR structures of $NtrC^r$ and P-$NtrC^r$ have been deposited in the Research Collaboratory for Structural Bioinformatics Protein Data Bank under the accession codes 1DC7 ($NtrC^r$) and 1DC8 (P-$NtrC^r$).

errata

A Chinese triconodont mammal and mosaic evolution of the mammalian skeleton

Ji Qiang, Luo Zhexi & Ji Shu-an

Nature **398,** 326–330 (1999)

The names of these authors are listed as the Chinese would write them and not according to *Nature*'s convention, that is with the family name first and the given name last. Correct citations of this paper should therefore refer to the authors as Ji, Q., Luo, Z.-X. and Ji, S.-A. □

Small-bandgap endohedral metallofullerenes in high yield and purity

S. Stevenson, G. Rice, T. Glass, K. Harich, F. Cromer, M. R. Jordan, J. Craft, E. Hadju, R. Bible, M. M. Olmstead, K. Maitra, A. J. Fisher, A. L. Balch & H. C. Dorn

Nature **401,** 55–57 (1999)

In the second paragraph on page 55, the third sentence is misleading and should read "The yields even exceed those of the empty-cage C_{84}" (without the erroneously inserted text "…the usually most abundant species…"). □

Saccharomyces cerevisiae telomerase is an Sm small nuclear ribonucleoprotein particle

Anita G. Seto, Arthur J. Zaug, Suzanne G. Sobel, Sandra L. Wolin & Thomas R. Cech

Nature **401,** 177–180 (1999)

The gel shown in Fig. 3a of this Letter should have had lanes 2–10 labelled I, S, B (in that order, three times, from left to right) for "input", "supernatant" and "bound", respectively. □

Human urotensin-II is a potent vasoconstrictor and agonist for the orphan receptor GPR14

Robert S. Ames, Henry M. Sarau, Johathan K. Chambers, Robert N. Willette, Nambi V. Aiyar, Anne M. Romanic, Calvert S. Louden, James J. Foley, Charles F. Sauermelch, Robert W. Coatney, Zhaohui Ao, Jyoti Disa, Stephen D. Holmes, Jeffrey M. Stadel, John D. Martin, Wu-Schyong Liu, George I. Glover, Shelagh Wilson, Dean E. McNulty, Catherine E. Ellis, Nabil A. Elshourbagy, Usman Shabon, John J. Trill, Douglas W. P. Hay, Eliot H. Ohlstein, Derk J. Bergsma & Stephen A. Douglas

Nature **401,** 282–286 (1999)

Units for the *x*-axis of Fig. 5b–g should be pmol kg^{-1} (and not nmol kg^{-1} as published). In Fig. 5f, the right numeral should be 1,000. □

© 1999 Macmillan Magazines Ltd

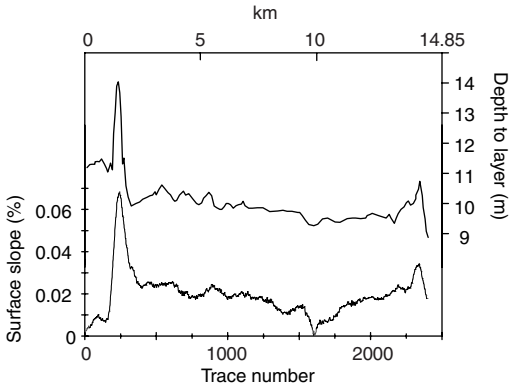

Figure 5 Comparison of accumulation rate with surface slope. The depth to a prominent internal horizon in Fig. 2b is taken as a proxy of accumulation rate. This depth is a good match to the magnitude of surface slope smoothed with a 120-m filter. Cross-correlation suggests that a 7% surface slope produces an accumulation rate ~30% higher than the regional average.

summit of Greenland was not supported by radar data[21,22]. The arches presented here are, to our knowledge, the first to be reported in the near-surface layers, at the divide, and the first to be shown to result from anomalous strain rate. We note that the width of these arches (1,570 ± 50 m) is approximately three times the ice thickness, which constitutes good agreement with Raymond's scaling analysis. The locus joining the crest of the arches tilts at −40° to the vertical, a probable indication of migration (0.5 m yr^{-1}) of the ice divide towards Rutford Ice Stream.

Although some benefits arise from collecting ice cores at ice divides, there are now at least two reasons to be wary of such sites; first, preferential wind-scouring which distorts isotopic ratios[23] and accumulation rates, and second, the possible presence of Raymond bumps. One precaution would be to ensure that flow models predicting depth–age relationships also reproduce the patterns in isochronous layers. Failure to account for Raymond bumps could incur substantial errors in accumulation-rate histories; for example, a hypothetical 100-m ice core from the crest of Fletcher Promontory would, unless corrected, yield erroneously low accumulation rates; an error of −2.6% at 10 m depth, −8% at 30 m and −26% at 100 m.

It is not yet clear over what length-scales and under what temperature conditions Raymond bumps form. But the presence of such bumps on Fletcher Promontory is a clear illustration of the nonlinear rheology of ice in a natural setting, which has often been questioned[24,25], and shows that special conditions can prevail beneath ice divides which should not be ignored when analysing even short ice cores. □

Received 16 April 1998; accepted 7 January 1999.

1. Robin, G. de Q. *The Climatic Record in Polar Ice Sheets* (Cambridge Univ. Press, 1983).
2. Clarke, T. S. & Bentley, C. R. High-resolution radar on Ice Stream B2, Antarctica: measurements of electromagnetic wave speed in firn and strain history from buried crevasses. *Ann. Glaciol.* **20,** 153–159 (1994).
3. Kohler, J., Moore, J., Kenet, M., Engeset, R. & Elvehøy, H. Using ground-penetrating radar to image previous year's summer surfaces for mass balance measurements. *Ann. Glaciol.* **24,** 255–260 (1997).
4. Raymond, C. F. Deformation in the vicinity of ice divides. *J. Glaciol.* **29,** 357–373 (1983).
5. Frolich, R. M. & Doake, C. S. M. SAR interferometry over Rutford Ice Stream and Carlson Inlet, Antarctica. *J. Glaciol.* **44,** 77–92 (1998).
6. Paren, J. G. & Robin, G. de Q. Internal reflections in polar ice sheets. *J. Glaciol.* **14,** 251–259 (1975).
7. Miners, W. D. *et al.* Forward modelling of the internal layers in radio echo sounding using electrical and density measurements from ice cores. *J. Phys. Chem. B* **101,** 6201–6204 (1997).
8. Harrison, C. H. Radio echo sounding of horizontal layers in ice. *J. Glaciol.* **12,** 383–397 (1973).
9. Black, H. P. & Budd, W. Accumulation in the region of Wilkes Land, Antarctica. *J. Glaciol.* **5,** 3–15 (1964).
10. Whillans, I. M. Effect of inversion winds on topographic detail and mass balance on inland ice sheets. *J. Glaciol.* **14,** 85–90 (1975).
11. Thomas, R. H., Stephenson, S. N., Bindschadler, R. A., Shabtaie, S. & Bentley, C. R. Thinning and grounding line retreat on the Ross Ice Shelf, Antarctica. *Ann. Glaciol.* **11,** 165–172 (1988).
12. Vaughan, D. G. Relating the occurrence of crevasses to surface strain rates. *J. Glaciol.* **39,** 255–267 (1993).
13. Dahl-Jensen, D. Two-dimensional thermo-mechanical modelling of flow and depth-age profiles near the ice divide in Central Greenland. *Ann. Glaciol.* **12,** 31–36 (1989).
14. Schøtt Hvidberg, C. Steady-state thermomechanical modelling of ice flow near the centre of large ice sheets with the finite-element technique. *Ann. Glaciol.* **23,** 116–123 (1996).
15. Weertman, J. Sliding-no sliding zone effect and age determination of ice cores. *Quat. Res.* **6,** 203–207 (1976).
16. Sandhäger, H. *Review of the Münster Airborne Radio-echo Sounding-data Set: Marine Ice beneath Filchner-Schelfeis; Bottom Reflectivity and Internal Structures of Berkner Island* 111–114 (Filchner-Ronne Ice Shelf Programe Rep. No. 9, Alfred-Wegener Inst., Bremerhaven, 1996).
17. Steinhage, D. & Blindow, N. *Results of Short Pulse Radio Echo Sounding on Thyssenhöhe, Berkner Island, Antarctica* 106–109 (Filchner-Ronne Ice Shelf Programme Rep. No. 10, Alfred-Wegener Inst. Bremerhaven, 1997).
18. Raymond, C. F. *et al.* Geometry and stratigraphy of Siple Dome, Antarctica. *Antarct. J. US* **30,** 91–93 (1995).
19. Nereson, N. A., Raymond, C. F., Waddington, E. D. & Jacobel, R. W. Recent migration of the Siple Dome ice divide, West Antarctica. *J. Glaciol.* **44,** 643–652 (1998).
20. Schøtt, C., Waddington, E. D. & Raymond, C. F. Predicted time-scales for GISP2 and GRIP boreholes at Summit, Greenland. *J. Glaciol.* **38,** 162–168 (1992).
21. Hempel, L. & Thyssen, F. Deep radio echo soundings in the vicinity of GRIP and GISP2 drill sites, Greenland. *Polarforschung* **62,** 11–16 (1992).
22. Jacobel, R. W. & Hodge, S. M. Radar internal layers from the Greenland summit. *Geophys Res. Lett.* **22,** 587–590 (1995).
23. Fisher, D. A. *et al.* Effect of wind scouring on climatic records from ice-core oxygen-isotope profiles. *Nature* **301,** 205–209 (1983).
24. Doake, C. S. M. & Wolff, W. W. Flow law for ice in polar ice sheets. *Nature* **314,** 255–257 (1985).
25. Wolff, E. W. & Doake, C. S. M. Implications of the form of the flow law for a vertical velocity and age-depth profiles in polar ice. *J. Glaciol.* **32,** 366–370 (1986).
26. Frolich, R. M., Vaughan, D. G. & Doake, C. S. M. Flow of Rutford Ice Stream and comparison to Carlson Inlet, Antarctica. *Ann. Glaciol.* **12,** 51–56 (1989).
27. Paterson, W. S. B. *The Physics of Glaciers* 3rd edn (Elsevier Science, Oxford, 1994).

Supplementary information is available on *Nature*'s World-Wide Web site and as paper copy from the London editorial office of *Nature*.

Acknowledgements. We thank C. Raymond, R. C. A. Hindmarsh, N. Nereson and colleagues at the British Antarctic Survey for their help and comments.

Correspondence and requests for materials should be addressed to D.G.V. (e-mail: d.vaughan@bas.ac.uk).

A Chinese triconodont mammal and mosaic evolution of the mammalian skeleton

Ji Qiang*†, Luo Zhexi‡ & Ji Shu-an*

** National Geological Museum of China, Beijing 100034, China*
† China University of Geosciences, Beijing 100083, China
‡ Section of Vertebrate Paleontology, Carnegie Museum of Natural History, Pittsburgh, Pennsylvania 15213-4080, USA

Here we describe a new triconodont mammal from the Late Jurassic/Early Cretaceous period of Liaoning, China. This new mammal is represented by the best-preserved skeleton known so far for triconodonts which form one of the earliest Mesozoic mammalian groups with high diversity. The postcranial skeleton of this new triconodont shows a mosaic of characters, including a primitive pelvic girdle and hindlimb but a very derived pectoral girdle that is closely comparable to those of derived therians. Given the basal position of this taxon in mammalian phylogeny, its derived pectoral girdle indicates that homoplasies (similarities resulting from independent evolution among unrelated lineages) are as common in the postcranial skeleton as they are in the skull and dentition in the evolution of Mesozoic mammals. Limb structures of the new triconodont indicate that it was probably a ground-dwelling animal.

Class Mammalia
Infraclass Triconodonta (McKenna and Bell 1997)
Order Eutriconodonta (Kermack *et al.* 1973)
Family *Incertae sedis*
Jeholodens jenkinsi gen. et sp. nov.

Etymology. Jehol: an ancient geographic name for the western part of the Liaoning Province, China; the namesake of the Jehol fauna in the Yixian Formation that yielded the holotype; *odens* (Latin): tooth; *jenkinsi* (Latin): in honour of F. A. Jenkins Jr for his pioneer studies of the evolutionary morphology of the mammalian post-cranial skeleton.

Holotype. GMV 2139 a, b, a nearly complete skeleton consisting of a partial skull and all of the postcranial skeleton preserved as two

© 1999 Macmillan Magazines Ltd

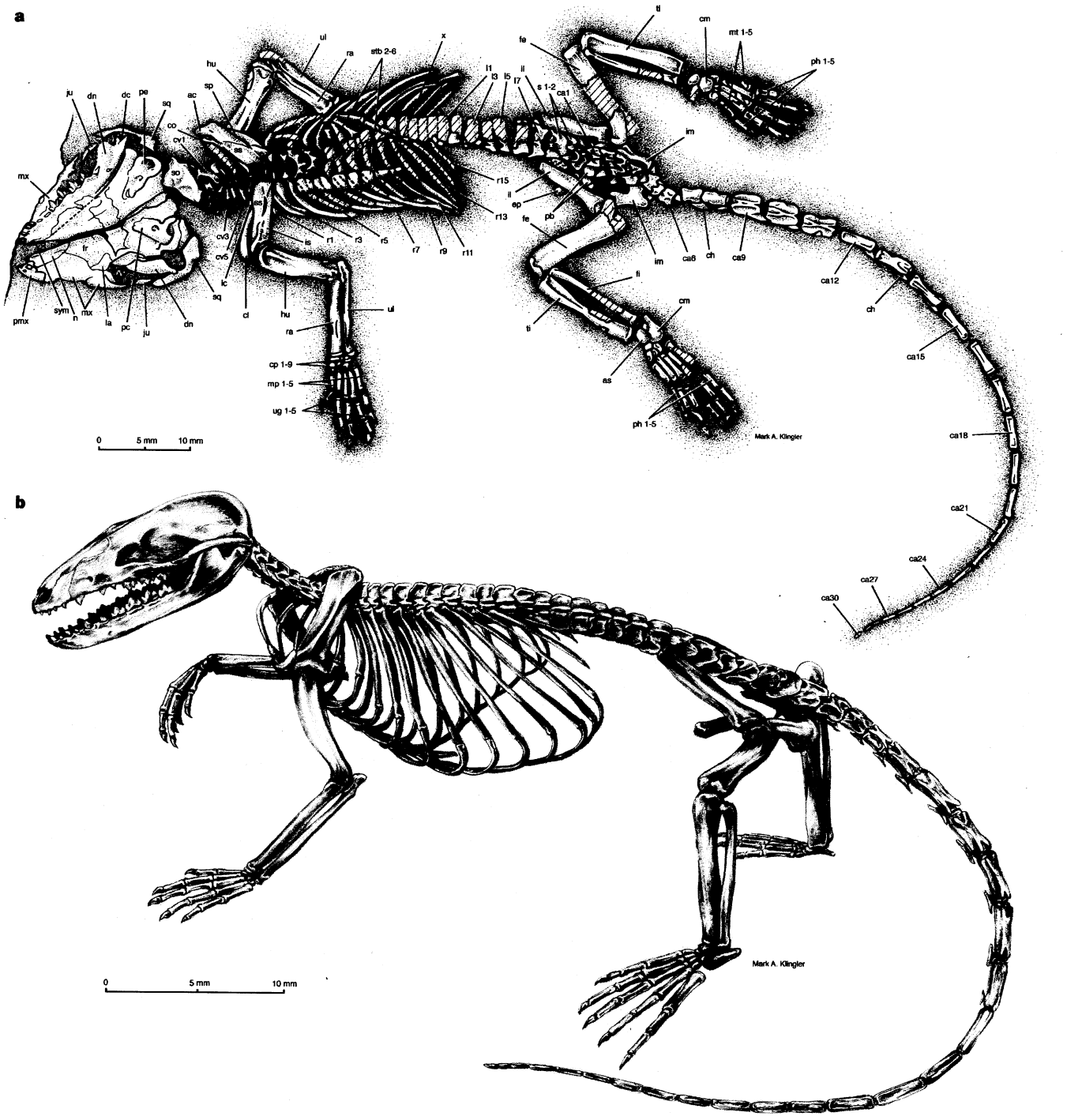

Figure 1 *Jeholodens jenkinsi* (National Geological Museum of China, holotype GMV 2139a). **a**, Dorsal view of the dorsoventrally compressed skeleton (dashed lines indicate impressions, for which the bone structures are almost completely preserved on the counterpart GMV 2139b, not shown). **b**, Reconstruction of *J. jenkinsi* as a ground-dwelling animal that had a plantigrade gait, sprawling hindlimbs and a mobile pectoral girdle with relatively wide range of excursion of the scapula but a sprawling elbow. Abbreviations: ac, acromion of scapula; as, astragalus; c, canine; c1–c7, cervical vertebrae 1–7; ca1–ca30, caudal vertebrae 1–30; ch, chevron (hemal arch); cl, clavicle; cm, calcaneum; co, coracoid process of scapula (or the unfused coracoid in cynodonts); cp1–cp9, carpals 1–9; dc, dentary condyle; dn, dentary; ep, epipubis; fe, femur; fi, fibula; fr, frontal; gl, glenoid of the scapula; hu, humerus; ic, interclavicle; il, ilium; im, ischium; is, infraspinous fossa (of scapula); i1–i4, incisors 1–4; i2r, replacement incisor 2; ju, jugal; la, lacrimal; L1–L7, lumbar vertebrae 1–7; ma, metacromion (on the spine of the scapula); mf, mandibular foramen; mg, meckelian groove; m1–4, molars 1–4; mp1–5, metacarpals 1–5; mt1–mt5, metatarsals 1–5; mx, maxillary; n, nasal; pb, pubic; pc, pars cochlearis of petrosal; pcd, coronoid process of dentary; pe, petrosal, preserved in the dorsal/endocranial view; pf, pterygoid fossa; ph1–5; phalanges 1–5; pmx, premaxillary; ps, pterygoid shelf on the ventral border of the mandible; p1, p2, premolars 1, 2; ra, radius; r1–r15, thoracic ribs 1–15; sc, scapula; sn, scapular notch; so, supraoccipital; sp, spine of scapula; sq, squamosal; ss, supraspinous fossa of scapula; stb2–6, sternebrae 2–6 (the interclavicle, the sternal manubrium and sternebra 1 are preserved and exposed by preparation, but are not shown in **a**); sym, mandibula symphysis; s1, s2, sacral vertebrae 1, 2; ti, tibia; tm, teres major fossa (on scapula); t1–t15, thoracic vertebrae 1–15; ug1–5, ungual phalanges 1–5; ul, ulna; x, xiphoid process of sternum.

© 1999 Macmillan Magazines Ltd

counterparts (Fig. 1a; a reconstruction of the specimen is shown in Fig. 1b).

Locality and horizon. The Sihetun site (at roughly 41° 40′ 12″ N, 120° 47′ 36″ E), about 32 km east of Chaoyang City, Liaoning Province, China. The holotype is from the lacustrine shales that are intercalated with neutrobasic volcanic beds in the Yixian Formation.

Geological age and fauna. Correlation of the Yixian Formation is equivocal. It has been suggested to be Late Jurassic[1], near the Jurassic–Cretaceous boundary[2–4], or Early Cretaceous[5]. The associated fauna includes the theropods *Sinosauropteryx*[1,4], *Protarchaeopteryx*[5], *Caudipteryx*[5], the birds *Confusiusornis* and *Liaoningornis*[2], the pterosaur *Eosipterus*, the mammal *Zhangheotherium*[3], and diverse fossil fishes, invertebrates and plants.

Diagnosis. Dental formula 4·1·2·3/4·1·2·4 (incisors, canine, premolars, molars); linguobuccally compressed molars with three main cusps in a straight alignment (Fig. 2a, b); uniquely derived among triconodonts in possessing spoon-shaped incisors (Fig. 2c). *Jeholodens jenkinsi* differs from morganucodontids in lacking the molar-interlocking mechanism (by cingular cuspule e and cusp b) found in morganucodontids[6–8], in having weak labial cingula of the upper molars (Fig. 2a), in lacking lower cingular cuspules e, f and g (kuhneocone), and in lacking the angular process and the postdentary trough on the mandible (Fig. 2c). In *J. jenkinsi*, lower molar cusp a occludes into the valley-groove between cusps A and B of the opposite upper molar, thus differing from amphilestids and gobiconodontids[9,10], in which lower cusp a occludes into the embrasure anterior to upper cusp B. *J. jenkinsi* also lacks cingular cuspules e and f in the lower molars of the latter groups. The lower molars are interlocked, with a crescent-shaped distal cusp d of the preceding molar fitted into the concave mesial margin of cusp b of the succeeding molar, which is diagnostic of the Triconodontidae[11–14]. The main cusp, a, of the new taxon is much higher than cusps b and c, a primitive character that is absent in triconodontids[11–15]. *J. jenkinsi* differs from most triconodontids, other than *Alticonodon*[11] and *Ichthyoconodon*[14], in lacking the continuous lingual cingulum on the lower molars; it differs from *Alticonodon* and *Ichthyoconodon* in having a shelf-like cusp d.

Lower incisor i_2 is about to be replaced by an erupting tooth (labelled i2r in Fig. 2c) and m_4 is erupting in the holotype of *Jeholodens jenkinsi*. This dental replacement indicates that the individual probably had not reached a full adult stage. We interpret the cusp pattern and the occlusion of laterally compressed molars in *J. jenkinsi* to be indicative of an insectivorous diet.

A noteworthy skeletal feature of this new taxon is a highly derived scapula (Figs 1a, 3a), confirming an earlier observation of a triconodontid from the Cretaceous of Montana[12]. It has a robust, peg-like acromion and a low elevation on the spine that resembles the metacromion of *Didelphis* (Fig. 3f); the supraspinous fossa is fully developed. The dorsal part of the scapula has a prominent triangular area (Figs 1 and 3), similar to the large attachment area for the teres major muscle in monotremes[16], a condition also present in the archaic therian *Zhangheotherium*[3]. The clavicle is curved. Its lateral end has a tapering point with a reduced contact to the acromion, whereas in living monotremes the two structures have a rigid and broad articulation. This suggests that *Jeholodens* had a mobile scapuloclavicular articulation. Medially, the clavicle has a limited overlap with the lateral process of the interclavicle, and lacks the rigid claviculointerclavicle articulation found in the tritylodont reptiles[16] and monotremes[17]. We interpret this joint to have had at least some degree of mobility, like the conditions in multituberculates[18–20] and in archaic[3] and living[21] therians.

The distal end of the humerus bears the radial and ulnar condyles on its anterior aspect, an incipient ulnar trochlea on its posteroventral aspect, and reduced ectepicondyles and entepicondyles (on the counterpart slab; not shown), like the condition in *Zhangheotherium*[3]. These features differ from the primitive condition in cynodonts[22], morganucodontids[23], multituberculates[18–20]

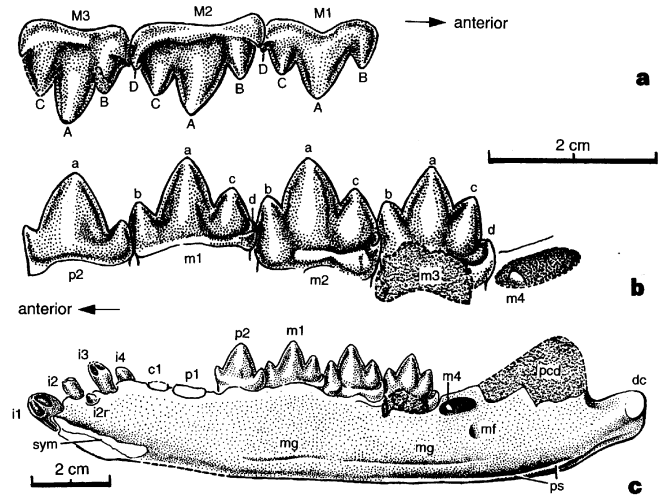

Figure 2 Dentition and mandible of *J. jenkinsi*. **a**, Upper molars M^{1-3} (right side labial view). **b**, Lower postcanines p_2–m_4 (right side, lingual view; m_4 is in the process of eruption). **c**, Mandible (right side, lingual view, corrected for slight distortion in the original specimen). Upper molars are labelled in the figure as M1–M3. Lower teeth are labelled as m1–m4; p1, p2, i1–i4 and i2r. We follow ref. 7 for the designation of cusps A–D on the upper molars and cusps a–d on the lowers. For other abbreviations see Fig. 1 legend. An analysis of mandibular and dental characters is found in Supplementary Information.

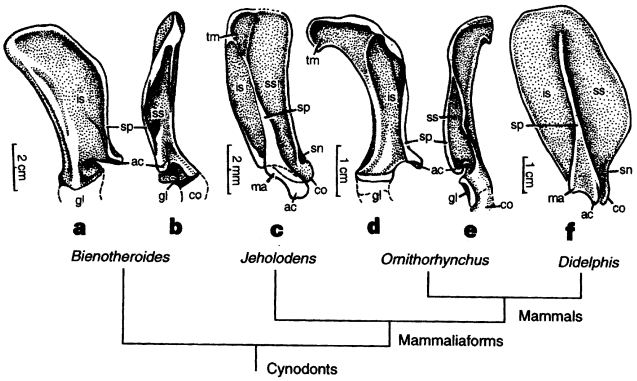

Figure 3 Mosaic evolution of the scapular characters in non-mammalian cynodonts and major mammalian clades. **a**, **b**, The tritylodontid *Bienotheroides* (lateral and anterior views of right scapula, after ref. 16, representing the outgroup condition of cynodonts[22]. **c**, *J. jenkinsi* (lateral view, right scapula, composite reconstruction from both left and right scapulae of holotype GMV 2139 a). **d**, **e**, The monotreme *Ornithorhynchus* (Carnegie Museum specimen CM 1478; lateral and anterior views of right scapula). **f**, The marsupial *Didelphis* (lateral view, right scapula). For abbreviations, see Fig. 1 legend. Given the phylogeny in Fig. 5 and those of other references[3,27], the following derived characters of the pectoral girdle and forelimb of *J. jenkinsi* and therian mammals (including *Zhangheotherium*) would be best interpreted as convergences: a full supraspinous fossa; a protruding and laterally positioned acromion; coracoid fused to scapula; a ventral and uniformly concave scapular glenoid; mobile claviculoscapular and clavicle–interclavicle joints; a greatly reduced interclavicle; reduced ectepicondyles and entepicondyles of humerus; an incipient trochlea of humerus for the ulna. Alternatively, if the features of *J. jenkinsi* and therians are regarded as primitive for mammaliaforms as a whole, then those similarities between *Ornithorhynchus* and the outgroup tritylodonts would have to be interpreted as atavistic reversals in *Ornithorhynchus* to those of cynodonts; such features include: weak supraspinous fossa on the anterior aspect of scapula; acromion on the anterior margin of scapula; a lateral and saddle-shaped glenoid; and rigid and broad articulations of the clavicle–interclavicle and the scapula–clavicle. In either scenario, homoplasies are prominent in features of the pectoral girdles and forelimbs[8,19,22]. Clade ranks following ref. 27; see also the alternatives given in refs 8, 29.

© 1999 Macmillan Magazines Ltd

and living monotremes, in which the humerus has no ulnar trochlea. The epiphyseal suture is not present in the long bones in the holotype of *J. jenkinsi*.

In contrast to the derived forelimb and pectoral girdle of *Jeholodens jenkinsi*, its pelvic girdle, hindlimb and pes share many plesiomorphic characters with morganucodontids[23], tritylodontids[16] and other cynodonts[22]. The epipubis is present. The patellar groove on the distal femur is far less developed than in monotremes, multituberculates and therians. The calcaneum (Fig. 4b) has a very short tubercle, a broad anterolateral ('peroneal') shelf, and extensive fibular and tibial facets, all of which are identical to those of morganucodontids[23] and non-mammalian cynodonts[22], but different from the distinct peroneal process in monotremes, multituberculates[18,19] and therians[24] and from the elongate tubercle of multituberculates and therians. The astragalus has a broad and uniformly convex tibial facet, but a weakly developed neck and navicular facet. The astragalus and calcaneum contact each other in juxtaposition; this condition is similar to that in non-mammalian cynodonts[22] and morganucodontids[23], but different from the partial overlap of these two ankle bones in multituberculates and the complete overlap of these bones in archaic[24] and living therians (Fig. 4). Metatarsal 5 is offset from the cuboid (Fig. 4), allowing a wide range of abduction of the lateral pedal digits, as in morganucodontids[23], monotremes and multituberculates[19]. The manual and pedal ungual phalanges are slightly curved dorsally and concave on both sides, similar to those of most ground-dwelling small mammals[19,25]. A flexor tubercle on the midpoint in most of the ungual phalanges indicates a certain degree of ability to flex the claws. *J. jenkinsi* lacks the sesamoid ossicle(s) of the monotremes, multituberculates and therians. We interpret *J. jenkinsi* to have been a ground-dwelling small mammal with a plantigrade gait (Fig. 1b) and some capability for climbing on uneven substrates[23], but not an arboreal mammal.

The eutriconodonts first appeared in the Middle Jurassic[15] and were quite diverse, with a worldwide distribution, in the Cretaceous[9–14]. Although abundantly represented by teeth[9–15] and some cranial[12,15,26] and postcranial[9] materials, no fully articulated skeleton was known, until now, for this diverse group. In traditional classifications of early mammals that were based primarily on dentition[6,12,15], eutriconodonts and morganucodontids belonged to the order Triconodonta. The traditional grouping of 'triconodonts' (morganucodontids + eutriconodonts) is considered to be a grade, rather than a monophyletic group, according to more recent phylogenetic analyses[26–28]. Studies of some dental and cranial characters indicate that eutriconodonts may also be a heterogeneous group[10,28].

It has been proposed that the postcranial features of cynodonts and early mammals were subjected to functional constraints of locomotion and therefore susceptible to homoplasies[19,22,29]. Several cladistic studies of cynodonts and early mammals that incorporated postcranial characters[27,30] indicated that dental characters are highly homoplastic, whereas the postcranial characters can be very informative for higher-level phylogeny. Because of the paucity of the relatively complete postcrania of the basal mammals, it is unknown whether (or to what degree) homoplasies exist among different postcranial skeletal parts (such as the forelimb versus the hindlimb) in early mammalian evolution.

The discovery of the first fully articulated triconodont skeleton offers an unprecedented opportunity for a more comprehensive assessment of the relationships of triconodonts, combining all evidence of the dentition, basicranium and postcranium, and will also allow us to elucidate the pattern of postcranial evolution in early mammals. Our phylogenetic analysis has placed *J. jenkinsi* in the basal part of the mammalian phylogenetic tree, outside the crown group of extant Mammalia (Fig. 5). Available evidence indicates that *J. jenkinsi* is a eutriconodont and far more derived than morganucodontids. Within eutriconodonts, the new taxon is more closely related to the triconodontid clade than it is to amphilestids and gobiconodontids (see Supplementary Information). These results are consistent with the ideas that triconodonts are paraphyletic[26–28] and that the triconodont-like molar cusp and occlusal patterns are characters for a functional grade.

Jeholodens jenkinsi shows a mosaic of derived, therian-like characters for most parts of the pectoral girdle (Fig. 3) and the humerus, but very primitive characters for the vertebral column, pelvic girdle, hindlimb and pes (Fig. 4). Our phylogenetic analysis indicates that many apomorphies of the pectoral girdle and forelimb in *J. jenkinsi* are independently derived and convergent with those of therians. Such apomorphies include a fully developed supraspinous fossa, the acromion and metacromion on the scapular spine, the incipient ulnar trochlea and the reduced epicondyles of the humerus. Given the phylogeny shown in Fig. 5, the mobile clavicle and scapula in *J. jenkinsi* would represent convergences with those of the multituberculate–therian clade[3,20,27]. Thus these pectoral

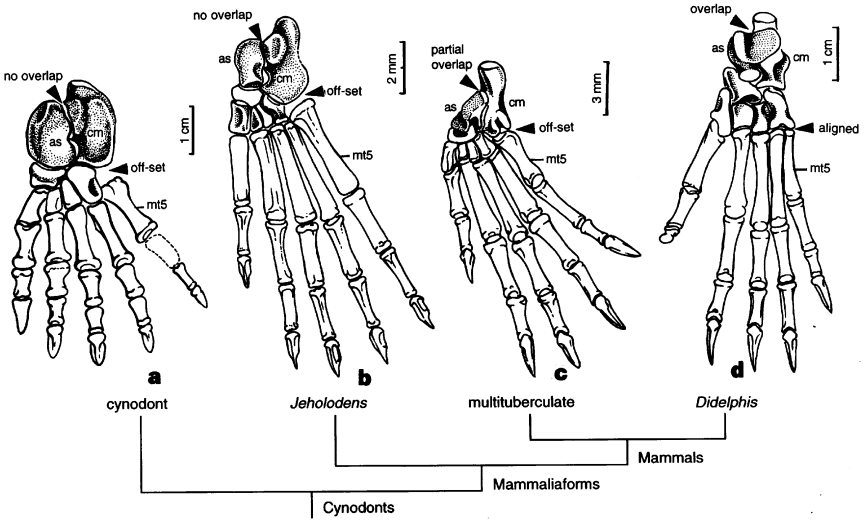

Figure 4 Pedes of mammals and outgroup cynodonts. **a**, A generalized cynodont condition (after refs 22, 28). **b**, *J. jenkinsi* (composite reconstruction of holotype GMV 2139 a,b). **c**, The multituberculate *Eucosmodon* (after refs 18, 19). **d**, The therian *Didelphis*. *J. jenkinsi* has little or no overlap of the astragalus and calcaneum, a primitive feature of cynodonts, contrasting with the partial overlap of these characters in multituberculates and the complete overlap in therians. Clade ranks follow ref. 27; see also the alternatives given in refs 8, 29.

© 1999 Macmillan Magazines Ltd

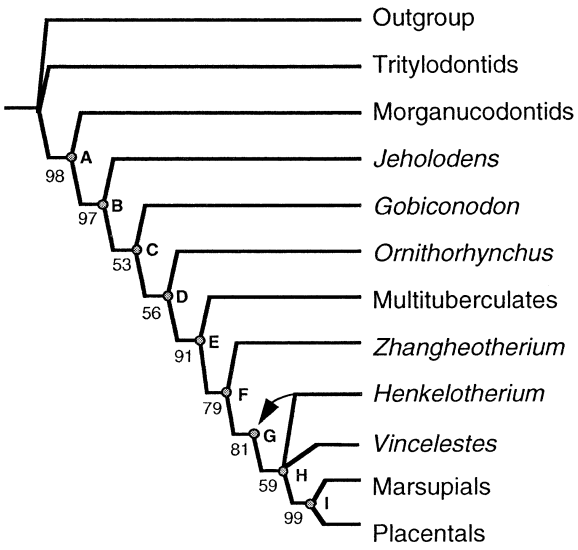

Figure 5 Evolutionary relationships of *J. jenkinsi*, gen. et sp. nov. The derived characters related to a mobile pectoral girdle occur separately on nodes B and E. The 'primitive' characters related to an immobile pectoral girdle occur in tritylodontids and the cynodont outgroup, and separately in *Ornithorhynchus* (node D). This indicates that there are many homoplasies of pectoral girdles and forelimbs (in contrast to the few or no convergences in the pelvic girdle and hindlimb), given the same tree topology of major clades of mammals. The arrow indicates an alternative placement of *Henkelotherium* at node G. For details of phylogenetic analysis see Methods and Supplementary Information.

characters, which allow a greater range of excursion of the shoulder joint in the locomotion of multituberculates[3,19,20] and living therians[21], have evolved at least twice among the Mesozoic mammals.

Alternatively, the mobile joints between the clavicle, interclavicle and scapula could be ancestral conditions shared by *J. jenkinsi* and the more derived mammals. If so, then the rigid clavicle–interclavicle articulation and relatively immobile scapula of monotremes (Fig. 3) would have to be regarded as atavistic reversals to the primitive conditions in the more distantly related non-mammalian cynodonts[16,22]. For either evolutionary scenario, we must conclude that the pectoral girdles and forelimbs of early mammals underwent extensive convergent evolution, not only by comparison with the dental and cranial features, but also in relation to more conservative features of the pelvis and hindlimbs. □

Methods

Phylogeny of mammals (Fig. 5) is based on a strict consensus of two equally parsimonious trees (tree length = 210; consistency index = 0.638; retention index = 0.724) from PAUP analysis (3.1.1. Branch and Bound search) of 101 dental, cranial and postcranial characters that can be scored for the 12 major clades of mammals (see Supplementary Information). Most of the characters are preserved in the holotype of *Jeholodens jenkinsi*. The two most pasimonious trees differ only in the alternative placements of *Henkelotherium*, which either is at node G (represented by an arrow in Fig. 5) or switches positions with *Vincelestes*. These alternative placements of *Henkelotherium* do not alter the positions of any other clades, including *J. jenkinsi*. Numbers on branches represent the percentage of bootstrap values in 1,000 bootstrap replicas for a 50% majority bootstrap consensus tree that has identical topology to one of the two most parsimonious trees (that in which *Henkelotherium* is positioned at node G).

Received 26 August 1998; accepted 27 January 1999.

1. Ji, Q. & Ji, S.-A. Discovery of the earliest bird fossils in China and the origin of birds. *Chinese Geol.* **1996,** 30–33 (1996).
2. Hou, L., Martin, L. D., Zhou, Z. & Feduccia, A. Early adaptive radiation of birds: evidence from fossils from Northeastern China. *Science* **274,** 1164–1165 (1996).
3. Hu, Y., Wang, Y., Luo, Z. & Li, C. A new symmetrodont mammal from China and its implications for mammalian evolution. *Nature* **390,** 137–142 (1997).
4. Chen, P.-J., Dong, Z.-M. & Zhen, S.-N. An exceptionally well-preserved theropod dinosaur from the Yixian Formation of China. *Nature* **391,** 147–152 (1998).
5. Ji, Q., Currie, P. J., Norell, M. A. & Ji, S.-A. Two feathered dinosaurs from northeastern China. *Nature* **393,** 753–761 (1998).
6. Kermack, K. A., Mussett, F. & Rigney, H. W. The lower jaw of *Morganucodon*. *Zool. J. Linn. Soc.* **53,** 87–175 (1973).
7. Crompton, A. W. The dentitions and relationships of the southern African Triassic mammals *Erythrotherium parringtoni* and *Megazostrodon rudnerae*. *Bull. Br. Mus. Nat. Hist.* **24,** 399–437 (1974).
8. Luo, Z. in *In the Shadow of Dinosaurs—Early Mesozoic Tetrapods* (eds Fraser, N. C. & Sues, H.-D.) 980–128 (Cambridge Univ. Press, Cambridge, 1994).
9. Jenkins, F. A. Jr & Schaff, C. R. The Early Cretaceous mammal *Gobiconodon* (Mammalia, Triconodonta) from the Cloverly Formation in Montana. *J. Vert. Paleontol.* **6,** 1–24 (1988).
10. Kielan-Jaworowska, Z. & Dashzeveg, D. New Early Cretaceous amphilestid ('triconodont') mammals from Mongolia. *Acta Palaeont. Polonica.* **43,** 413–438 (1998).
11. Fox, R. C. Additions to the mammalian local fauna from the upper Milk River Formation (Upper Cretaceous), Alberta. *Can. J. Earth Sci.* **13,** 1105–1118 (1976).
12. Jenkins, F. A. Jr & Crompton, A. W. in *Mesozoic Mammals: The First Two-thirds of Mammalian History* (eds Lillegraven, J. A., Kielan-Jaworowska, Z. & Clemens, W. A.) 74–90 (Univ. Calif. Press, Berkeley, 1979).
13. Cifelli, R. L., Wible, J. R. & Jenkins, F. A. Jr Triconodont mammals from the Cloverly Formation (Lower Cretaceous), Montana and Wyoming. *J. Vert. Paleontol.* **16,** 237–241 (1998).
14. Sigogneau-Russell, D. Two possibly aquatic triconodont mammals from the Early Cretaceous of Morocco. *Acta Palaeont. Polonica* **40,** 149–162 (1995).
15. Simpson, G. G. *A catalogue of the Mesozoic Mammalia in the Geological Department of the British Museum* (Oxford Univ. Press, London, 1928).
16. Sun, A. & Li, Y. The postcranial skeleton of the late tritylodont *Bienotheroides*. *Vert. PalAsiat.* **23,** 136–151 (1985).
17. Klima, M. Die Frühentwicklung des Schültergürtels und des Brustbeins bei den Monotremen (Mammalia: Prototheria). *Adv. Anat. Embryol. Cell Biol.* **47,** 1–80 (1973).
18. Krause, D. W. & Jenkins, F. A. Jr The postcranial skeleton of North American multituberculates. *Bull. Mus. Comp. Zool.* **150,** 199–246 (1983).
19. Kielan-Jaworowska, Z. & Gambaryan, P. P. Postcranial anatomy and habits of Asian multituberculate mammals. *Fossils Strata* **36,** 1–92 (1994).
20. Sereno, P. & McKenna, M. C. Cretaceous multituberculate skeleton and the early evolution of the mammalian shoulder girdle. *Nature* **377,** 144–147 (1995).
21. Jenkins, F. A. Jr & Weijs, W. A. The functional anatomy of the shoulder in the Virginia opossum (*Didelphis virginiana*). *J. Zool.* **188,** 379–410 (1979).
22. Jenkins, F. A. Jr The postcranial skeleton of African cynodonts. *Bull. Peabody Mus. Nat. Hist. Yale Univ.* **36,** 1–216 (1971).
23. Jenkins, F. A. Jr & Parrington, F. R. Postcranial skeleton of the Triassic mammals *Eozostrodon*, *Megazostrodon*, and *Erythrotherium*. *Phil. Trans. R. Soc. Lond. B* **273,** 387–431 (1976).
24. Rougier, G. W. *Vincelestes neuquenianus* Bonaparte (Mammalia, Theria), un primitivo mammifero del Cretacico Inferior de la Cuenca Neuqina. Thesis, Univ. Nacional de Buenos Aires (1993).
25. McLeod, N. & Rose, K. D. Inferring locomotory behavior in Paleogene mammals via eigenshape analysis. *Am. J. Sci.* **293,** 300–355 (1993).
26. Rougier, G. W., Wible, J. R. & Hopson, J. A. Basicranial anatomy of *Priacodon fruitaensis* (Triconodontidae, Mammalia) from the Late Jurassic of Colorado, and a reappraisal of mammaliaform interrelationships. *Am. Mus. Novit.* **3183,** 1–28 (1996).
27. Rowe, T. Definition, diagnosis, and origin of Mammalia. *J. Vert. Paleontol.* **8,** 241–264 (1988).
28. Kielan-Jaworowska, Z. Characters of multituberculates neglected in phylogenetic analyses of early mammals. *Lethaia* **29,** 249–255 (1997).
29. Hopson, J. A. in *Major Features of Vertebrate Evolution* (eds Prothero, D. R. & Schoch, R. M.) 190–219 (Short Courses in Paleontol. No. 7, Paleontol. Soc. Knoxville, Tennessee, 1994).
30. Kemp, T. S. The relationships of mammals. *Zool. J. Linn. Soc.* **77,** 353–384 (1983).

Supplementary information is available on *Nature*'s World-Wide Web site (http://www.nature.com) or as paper copy from the London editorial office of *Nature*.

Acknowledgements. We thank K. C. Beard, R. L. Cifelli, W. A. Clemens, A. W. Crompton, M. R. Dawson, J. A. Hopson, F. A. Jenkins, Z. Kielan-Jaworowska, J. Meng, T. Rowe, D. Sigogneau-Russell, J. R. Wible and X.-c. Wu for discussions and for reviews of the manuscript; A. Henrici for preparation of the specimen; M. Klingler for preparing Fig. 1; and N. Wuethele for assistance. This research was supported by funding from the Ministry of Geology and Mineral Resources of China and the National Natural Science Foundation of China (to J.Q.), and the US National Science Foundation, the National Geographic Society, and the M. Graham Netting Fund of the Carnegie Museum (to Z.L.).

Correspondence and requests for materials should be addressed to: Z. Luo (e-mail: luoz@clpgh.org).

Strong effects of weak interactions in ecological communities

E. L. Berlow

Department of Integrative Biology, University of California, Berkeley, California 94720-3140, USA

The loss or removal of individual species can cause dramatic changes in communities[1–5]. Experiments indicate that in many communities only a few species will have such strong effects, whereas most will have weak effects owing to small *per capita* effects and/or low abundance[3,6–15,16]. But extinction of these 'weak' interactors could significantly alter natural communities because they play important stabilizing or 'noise-dampening' roles[14,15,17–23]. I

© 1999 Macmillan Magazines Ltd

Small-bandgap endohedral metallofullerenes in high yield and purity

S. Stevenson*, G. Rice*, T. Glass*, K. Harich*, F. Cromer*, M. R. Jordan*, J. Craft*, E. Hadju†, R. Bible†, M. M. Olmstead‡, K. Maitra‡, A. J. Fisher‡, A. L. Balch‡ & H. C. Dorn*

* *Department of Chemistry, Virginia Polytechnic Institute of State University, Blacksburg, Virginia 24061, USA*
† *G. D. Searle & Co., 5200 Old Orchard Road, Skokie, Illinois 60077, USA*
‡ *Department of Chemistry, University of California, Davis, California 95616, USA*

The idea[1] that fullerenes might be able to encapsulate atoms and molecules has been verified by the successful synthesis of a range of endohedral fullerenes, in which metallic or non-metallic species are trapped inside the carbon cage[2–13]. Metal-containing endohedral fullerenes have attracted particular interest as they might exhibit unusual material properties associated with charge transfer from the metal to the carbon shell. However, current synthesis methods have typical yields of less than 0.5%, and produce multiple endohedral fullerene isomers, which makes it difficult to perform detailed studies of their properties. Here we show that the introduction of small amounts of nitrogen into an electric-arc reactor allows for the efficient production of a new family of stable endohedral fullerenes encapsulating trimetallic nitride clusters, $Er_xSc_{3-x}N@C_{80}$ ($x = 0$–3). This 'trimetallic nitride template' process generates milligram quantities of product containing 3–5% $Sc_3N@C_{80}$, which allows us to isolate the material and determine its crystal structure, and its optical and electronic properties. We find that the Sc_3N moiety is encapsulated in a highly symmetric, icosahedral C_{80} cage, which is stabilized as a result of charge transfer between the nitride cluster and the fullerene cage. We expect that our method will provide access to a range of small-bandgap fullerene materials, whose electronic properties can be tuned by encapsulating nitride clusters containing different metals and metal mixtures.

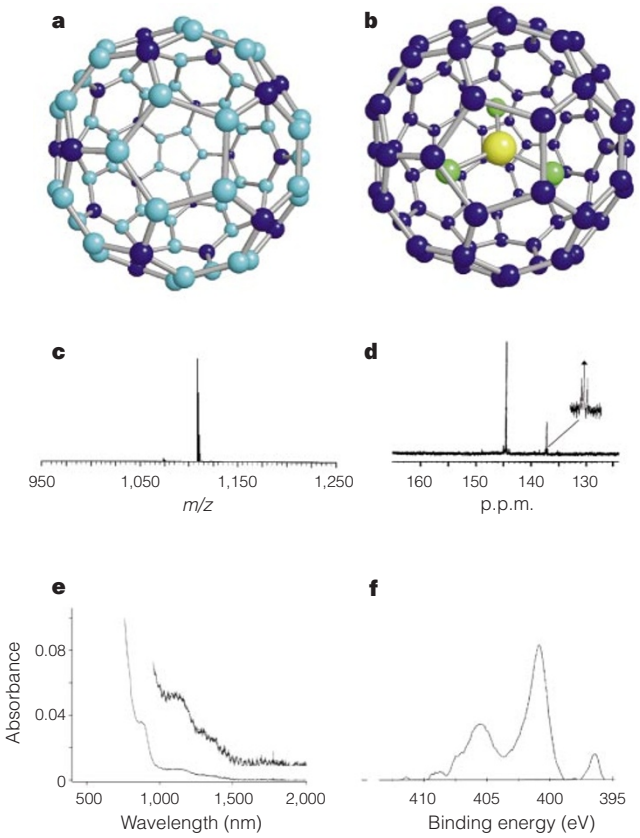

Figure 1 Structures and spectroscopic data for $Sc_3N@C_{80}$. **a**, Empty-cage fullerene, C_{80}, I_h isomer, showing pyrene (dark blue) and corannulene (light blue) sites; **b**, structure of $Sc_3N@C_{80}$. **c**, Negative ion-desorption chemical ionization (NI–DCI) mass spectrum for purified $Sc_3N@C_{80}$ (see Supplementary Information for mass spectral isotope data and HPLC purity trace). **d**, The 150 MHz ^{13}C NMR spectrum (17,130 scans, ~15 hours) for purified, ^{13}C-labelled (11%) $Sc_3N@C_{80}$ in CS_2/CrIII) acetylacetonate and referenced to tetramethyl silane (TMS). **e**, Ultraviolet-visible-near infrared spectrum for $Sc_3N@C_{80}$ in CS_2; inset, vertical expansion. **f**, X-ray photoelectron spectroscopy (XPS) spectrum of $Sc_3N@C_{80}$ evaporated on a Au film.

We have previously noted an unidentified scandium endohedral metallofullerene species (with a mass-to-charge ratio, *m/z*, of 1,109) in chromatographic fractions that were obtained from the extraction of scandium metallofullerene soot[14]. We now report that introduction of a small amount of N_2 gas into the Krätschmer–Huffman generator[15] results in significantly enhanced product of this species. The yields even exceed those of the usually most abundant species, the empty-cage C_{84}; with a single packed-graphite rod, the soluble fullerene and endohedral metallofullerene fraction (~60 mg) results in the isolation of 2–4 mg of the species with $m/z = 1109$ (see Methods for details on synthesis and isolation). The isotope patterns for the negative-ion mass spectra for natural abundance (Fig. 1c) and ^{13}C-enriched samples of this species are consistent with $Sc_3N@C_{80}$.

The structures of the empty icosahedral C_{80} cage and of $Sc_3N@C_{80}$ are shown in Fig. 1a and b, respectively, while the 150 MHz ^{13}C NMR spectrum for the ~11% ^{13}C enriched $Sc_3N@C_{80}$ sample is shown in Fig. 1d. As predicted for a C_{80} cage with I_h symmetry[8], the spectrum consists of only two resolved lines (at chemical shifts of 144.57 and 137.24 p.p.m.) with an intensity ratio of 3/1. This ^{13}C NMR spectrum contrasts with the single line reported by Akasaka *et al.*[13] for $La_2@C_{80}$; they interpreted their result in terms of rapid circular motion of the La atoms in a C_{80} cage with I_h symmetry. Fullerene carbon atoms at the intersection of three six-membered rings (6MR), pyrene-type sites (shown in dark blue in Fig. 1a), usually exhibit ^{13}C chemical shifts in the range 130–138 p.p.m. (ref. 16) which is consistent with the peak at 137.24 p.p.m. Carbon atoms at the intersection of one five-membered ring (5MR) and two 6MRs, corannulene sites (shown in light blue in Fig. 1a), are usually found in the range 138–145 p.p.m. which is consistent with the peak at 144.57 p.p.m. As expected, the observed ^{13}C–^{13}C spin–spin coupling pattern ($^1J_{C-C} = 57.2$ Hz) has the same satellite intensity for the doublets centred about the central peaks at 144.57 and 137.24 p.p.m. (3/1 intensity ratio). This result is consistent with a pyrene site (137.24 p.p.m.) bonded to three equivalent corannulene sites (Fig. 1a). The corannulene site (144.57 p.p.m.) exhibits coupling to only one adjacent pyrene site. The magnitude of this scalar coupling interaction (57.2 Hz) is similar to values reported for other fullerene sp^2–sp^2 hybridized carbons[17]. Our ^{13}C NMR results suggest that internal motion of the Sc_3N cluster yields a time-averaged electronic environment that preserves overall I_h symmetry for the carbon cage, with the encapsulated Sc_3N cluster not localized at specific internal bonding sites (on the NMR timescale at 295 K). An ambient temperature, the ^{45}Sc NMR spectrum for $Sc_3N@C_{80}$ exhibits a single symmetric line which is also indicative of a dynamic structure (see Supplementary Information). A unique feature of the C_{80} cage, with I_h symmetry, is the absence of bonding between two different 5MRs as illustrated by the isolated 5MRs (light blue) in Fig. 1a. These bonded sites between 5MRs are usually the most reactive in common fullerene cages (C_{60}, C_{70} and C_{84}) and a different chemical reactivity pathway will be necessary for $Sc_3N@C_{80}$ (ref. 18). Almost all fullerenes react with inorganic and organic reagents by addition to 6:6 ring junctions between two pentagons. These are absent in I_hC_{80}.

© 1999 Macmillan Magazines Ltd

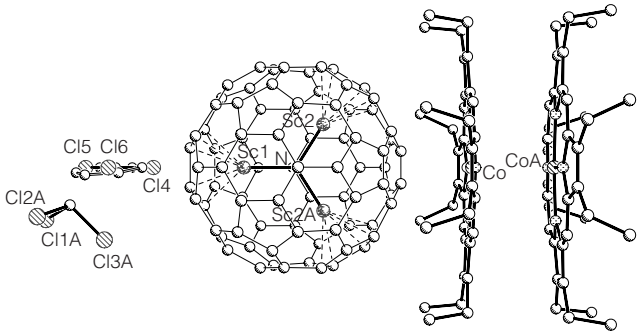

Figure 2 The structure of $(Sc_3N@C_{80})\cdot Co^{II}(OEP)\cdot 1.5\ CHCl_3\cdot 0.5\ C_6H_6$, perpendicular to the crystallographic mirror plane that bisects Co, Sc1 and N. The porphyrin portion has normal distances and angles. Only the main orientation (0.75 fractional occupancy) of the Sc_3N portion is shown. Bond distances (Å): N–Sc1, 2.011(19); N–Sc2, 1.966(12); shortest C–Sc, 2.188(9), 2.170(10). Angles (deg): Sc1–N–Sc2, 122.2(6); Sc2–N–Sc2A, 115.5(11). Benzene and chloroform (Cl4–Cl6) molecules are randomly distributed over a common site in a 1:3 ratio.

The central electronegative nitrogen atom in the Sc_3N cluster significantly alters other properties of this new family of endohedral metallofullerenes. It has been established[19,20] that the chromatographic retention parameter k ($= t_r/t_0$ = retention time/void time) is proportional to the polarizability and number of π-electrons at the fullerene cage surface for non-polar chromatographic stationary phases such as 2-(1-pyrenyl)ethyl (PYE), pyrenylethyl, and pentabromobenzyl (PBB)[19,20]. $La_2@C_{80}$ on a PBB stationary phase (toluene solvent) has, for example, a reported[21] elution time corresponding to that observed for empty-cage C_{88}–C_{90} whereas $Sc_3N@C_{80}$ elutes together with C_{84}–C_{86} under the same conditions. The different behaviour of $Sc_3N@C_{80}$ corresponds to a decrease of approximately four π-electrons at the fullerene cage surface relative to $La_2@C_{80}$ and suggests significant electron withdrawal from the carbon cage surface by the central nitrogen atom.

Although the electronic spectra of most endohedral metallofullerenes are dominated by features of the carbon cage rather than the encapsulated metals, the spectrum of the Sc_3N cluster indicates significant perturbation of the carbon cage. The ultraviolet-visible-near infrared spectrum of $Sc_3N@C_{80}$ (Fig. 1e) consists of significant absorption beyond 1,000 nm, and prominent peaks at 900 and 1,140 nm. If the absorption onset corresponds to the bandgap energy, the onset for $Sc_3N@C_{80}$ (at ~1,560 nm) corresponds to a bandgap of only 0.8 eV. The absorption onset for $La_2@C_{80}$ is significantly higher in energy (~1,000 nm, 1.3 eV), and is consistent with the larger bandgap reported for this endohedral species[21,22]. The X-ray photoelectron spectroscopy (XPS) spectrum for $Sc_3N@C_{80}$ (Fig. 1f) has an absorption at ~400.9 eV for the $2p_{3/2}$Sc core level, and a second peak (due to spin–orbital coupling) 4.8 eV higher in energy that is consistent with other scandium endohedral species. A small nitrogen peak is observed at 396.4 eV. The scandium and nitrogen XPS signal areas (corrected for relative sensitivities) indicate a 3/1 Sc/N ratio for the cluster. In addition, the binding energy for the nitrogen peak (396.4 eV) compares favourably with the value reported for scandium nitride[23], 396.2 eV.

We confirmed the endohedral nature of $Sc_3N@C_{80}$ by a single-crystal X-ray diffraction study of $(Sc_3N@C_{80})\cdot Co^{II}(OEP)\cdot 1.5\ CHCl_3\cdot 0.5\ C_6H_6$. Discrepancies between observed and calculated data remain, but appear to be accounted for by the presence of different orientations of the C_{80} cage. (See Methods and Supplementary Information for details). Figure 2 shows the structure, with the planar Sc_3N unit clearly encapsulated within the C_{80} cage. The $Sc_3N@C_{80}$ molecule is close to (but not covalently bound to) the $Co^{II}(OEP)$ molecule, which makes face-to-face contact with another $Co^{II}(OEP)$ moiety, as seen in related compounds[24]. The N–Sc distances, 2.011 (±0.019), 1.966(±0.012) Å, are slightly shorter than the Sc–N bonds in amide compounds such as $\{(HSiMe_2)_2N\}_3Sc(THF)$ (average Sc–N distance, 2.069 Å)[25]. In the solid, the scandium ions face three pentagons within the C_{80} cage.

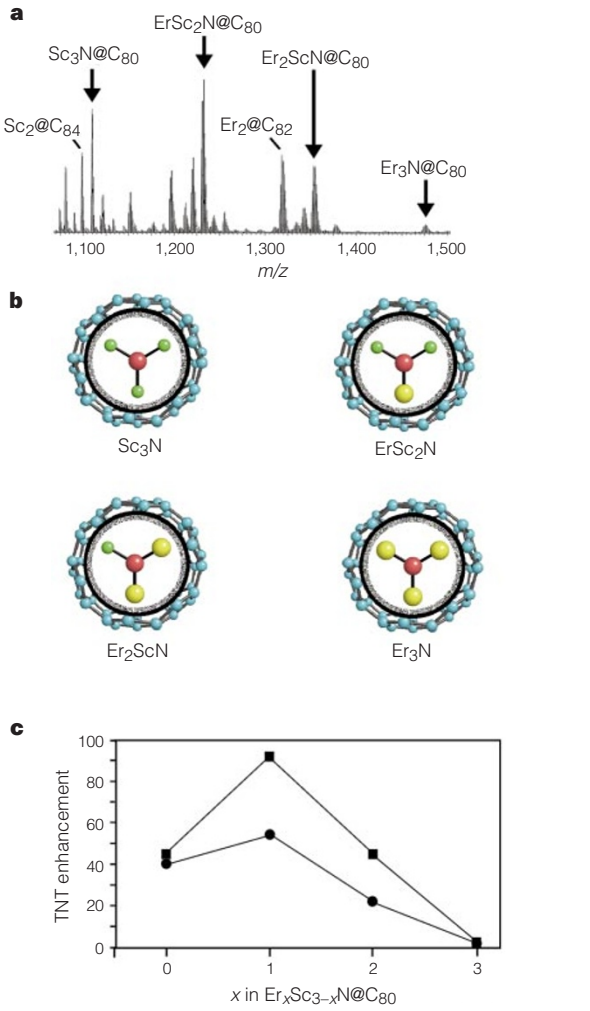

Figure 3 Mass spectral data for $Er_{3-x}Sc_xN@C_{80}$ formation. **a**, The NI-DCI mass spectrum for the mixed scandium and erbium endohedral metallofullerene chromatographic fraction after the first automated PBB/carbon disulphide separation stage. This fraction was maximized to illustrate all species (see Supplementary Information) for mass spectral isotope data. **b**, The pictorial cut-out representation of $Sc_3N@C_{80}$, $ErSc_2N@C_{80}$, $Er_2ScN@C_{80}$ and $Er_3N@C_{80}$. **c**, Plot showing the higher yields obtained with our 'trimetallic nitride template' (TNT) process. Data are shown for graphite rods packed with two different metal loadings, distinguished by their Er_2O_3/Sc_2O_3/powdered graphite ratio: filled circles, 1.5/1.5/97; filled squares, 3/3/94. The yields obtained from the mass spectral data are internally referenced to the well known trimetallic endohedral[14], $Sc_3@C_{82}$, which is also formed in the absence of nitrogen (not formed via the TNT process). Yields were determined from NI-DCI mass spectrometry.

Graphite rods were also packed with an Er_2O_3/Sc_2O_3/powered graphite mixture, and vaporized in similar fashion in the Krätschmer–Huffman generator. In Fig. 3a we show the negative ion-desorption chemical ionization mass spectrum for the chromatographic fraction after the first automated PBB/carbon disulphide separation stage (see Methods) which corresponds to elution times for empty-cage C_{82}–C_{86} species. All members of the $Er_xSc_{3-x}N@C_{80}$ ($x = 0$–3) family are present in this fraction (see also Fig. 3b). The higher yields with our 'trimetallic nitride template' process are illustrated in Fig. 3c for graphite rods packed with two different metal loadings. $Sc_3N@C_{80}$, $Er_2ScN@C_{80}$ and $ErSc_2N@C_{80}$ are all formed in yields that are 1–2 orders of magnitude greater than $Sc_3@C_{82}$. Besides the previously described $Er_2@C_{82}$ and $Sc_2@C_{84}$

© 1999 Macmillan Magazines Ltd

species[3,26], the mixed metal endohedrals ErSc@C_{82} and ErSc@C_{84} also appear to be members of this fraction, but at nearly the same levels as the usually prominent endohedral, Sc_2@C_{84}. □

Methods

Synthesis and isolation.

Graphite rods filled with Sc_2O_3/graphite (3 wt%/97 wt%) were vaporized in a Krätschmer–Huffman generator[15] in a dynamic helium atmosphere (300 torr) containing a small amount of nitrogen (1–3 torr). A single rod typically yields 60 mg soluble fullerenes and endohedral metallofullerenes, which are extracted from the soots using carbon disulphide. Following extraction of the fullerene and metallofullerene containing soots, the ^{13}C-labelled and natural-abundance extracts were filtered through glass wool. The initial automated chromatographic separation stage utilized a pentabromobenzyl column (PBB, 25 cm × 10 mm inside diameter; Phenomenex Co., Torrance, California, USA) with CS_2 as the mobile phase (2 ml min^{-1}). In the second and third stages, a selective semi-preparative Trident-Tri-DNP (di-nitrophenyl) column (Buckyclutcher, 25 cm × 10 mm inside diameter, Regis Chemical, Morton Grove, Illinois, USA) was utilized with toluene as the solvent (2 ml min^{-1}). The final purification stage involved separation with the PBB column (CS_2 mobile phase, 2 ml min^{-1}). Carbon disulphide solutions of Sc_3N@C_{80} (solubility, ~2 mg ml^{-1}) are reddish-brown. Sc_3N@C_{80} is soluble in other non-polar solvents (toluene, decalin), but has no significant solubility in more polar solvents (diethyl ether, acetone, methanol).

X-ray analysis.

The X-ray diffraction study was performed on (Sc_3N@C_{80})·Co^{II}(OEP)·1.5 $CHCl_3$·0.5 C_6H_6, which was obtained by mixing a solution of Sc_3N@C_{80} in benzene/carbon disulphide with a solution of Co_{II}(OEP) (OEP is the dianion of octaethylporphyrin) in chloroform. Crystal data as follows. fw = 1,919.48, dark red parallelepiped, 0.02 × 0.02 × 0.02 mm, monoclinic, space group $C2/m$, a = 25.142(5) b = 15.246(3), c = 19.459(3) Å, β = 94.79(3)°, V = 7433(3) Å^3, λ = 1.54178 Å, Z = 4, D_c = 1.715 Mg m^{-3}; μ(Cu–Kα) = 6.012 mm^{-1}; $2\theta_{max}$ = 113°; T = 130 K; 9,878 refl. collected; 5,138 independent (R_{int} = 0.112) included in the refinement; no absorption correction performed; programs used for solution and refinement, SHELXS-97 (ref. 27); full-matrix least squares based on F^2, SHELXL-97 (ref. 27); 312 parameters, R1 = 0.2730, wR2 = 0.5932 for all data; R1 = 0.2244 computed for 3,781 observed data (>2σ(I)). The R values did not fall to satisfactory levels. Difference Fourier maps suggest that the discrepancy resides in electron density in the region of the C_{80} cage, and that other orientations of the cage are also present (see Supplementary Information for further details).

Received 22 March; accepted 19 July 1999.

1. Kroto, H. W., Heath, J. R., O'Brien, S. C., Curl, R. F. & Smalley, R. E. Buckminsterfullerene. *Nature* **318,** 162–163 (1985).
2. Chai, Y. *et al.* Fullerenes with metals inside. *J. Phys. Chem.* **95,** 7564–7560 (1991).
3. Beyers, R. *et al.* Preparation and structure of the metallofullerene Sc_2@C_{84}. *Nature* **370,** 196–199 (1994).
4. Bethune, D. S., Johnson, R. D., Salem, J. R., de Vries, M. S. & Yannoni, C. S. Atoms in carbon cages: the structure and properties of endohedral fullerenes. *Nature* **366,** 123–128 (1993).
5. Nagase, S., Kobayashi, K. & Akasaka, T. in *Fullerenes: Recent Advances in the Chemistry and Physics of Fullerenes and Related Materials* (eds Kadish, K. M. & Ruoff, R. S.) 747–762 (Electrochemical Society, Pennington, 1995).
6. Nagase, S., Kobayashi, K. & Akasaka, T. Endohedral metallofullerenes: new spherical cage molecules with interesting properties. *Bull. Chem. Soc. Jpn* **69,** 2131–2142 (1996).
7. Manolopoulous, D. E. & Fowler, P. W. Structural proposals for endohedral metal-fullerene complexes. *Chem. Phys. Lett.* **187,** 17 (1991).
8. Fowler, P. W. & Manoloupoulos, D. E. An Atlas of Fullerenes (Oxford Univ. Press, 1995).
9. Heinrich, F. H. *et al.* Isolation and characterization of C_{80}. *Angew. Chem. Int. Edn Engl.* **35,** 1732–1734 (1996).
10. Wang, C.-R., Dennis, J. S., Inakuma, M. & Shinohara, H. in *Fullerenes: Recent Advances in the Chemistry and Physics of Fullerenes and Related Materials* (eds Kadish, K. M. & Ruoff, R. S.) 1023–1030 (Electrochemical Society, Pennington, 1998).
11. Kobayashi, K. & Nagase, S. Structures and electronic states of endohedral dimetallofullerenes: M_2@C_{80} (M = Sc, Y, La, Ce, Pr, Eu, Gd, Yb, and Lu). *Chem. Phys. Lett.* **262,** 227–232 (1996).
12. Kobayashi, K., Nagase, S. & Akasaka, T. Endohedral dimetallofullerenes Sc_2@C_{84} and La_2@C_{80}. Are the metal atoms still inside the fullerene cages? *Chem. Phys. Lett.* **261,** 502–506 (1996).
13. Akasaka, T. *et al.* ^{13}C and ^{139}La NMR studies of La_2@C_{80}: first evidence for circular motion of metal atoms in endohedral metallofullerenes. *Angew. Chem. Int. Edn Engl.* **36,** 1643–1645 (1997).
14. Stevenson, S. *et al.* Automated HPLC separation of endohedral metallofullerene Sc@C_{2n} and Y@C_{2n} fractions. *Anal. Chem.* **66,** 2675–2679 (1994).
15. Krätschmer, W., Fostiropoulos, K. & Huffman, D. R. The infrared and ultraviolet absorption spectra of laboratory-produced carbon dust: evidence for the presence of the C_{60} molecule. *Chem. Phys. Lett.* **170,** 167–170 (1990).
16. Diederich, F. & Whetten, R. L. Beyond C_{60}: the higher fullerenes. *Acc. Chem. Res.* **25,** 119–126 (1992).
17. Johnson, R. D., Meier, G., Salem, J. R. & Bethune, D. S. 2D nuclear magnetic resonance study of the structure of the fullerene C_{70}. *J. Am. Chem. Soc.* **113,** 3619–3621 (1991).
18. Hirsch, A. *The Chemistry of the Fullerenes* (Thieme Verlung, Stuttgart, 1994).
19. Fuchs, D. *et al.* Extraction and chromatographic elution behavior of endohedral metallofullerenes: inferences regarding effective dipole moments. *J. Phys. Chem.* **100,** 725–729 (1996).
20. Stevenson, S. *et al.* La_2@C_{72}: metal-mediated stabilization of a carbon cage. *J. Phys. Chem.* **102,** 2833–2837 (1998).
21. Yamamoto, K., Ishiguro, T., Sakurai, K. & Funasaka, H. in *Fullerenes: Recent Advances in the Chemistry and Physics of Fullerenes and Related Materials* (eds Kadish, K. M. & Ruoff, R. S.) 743–753 (Electrochemical Society, Pennington, 1997).
22. Kikuchi, K., Nakao, Y., Achiba, Y. & Nomura, M. in *Fullerenes: Recent Advances in the Chemistry and Physics of Fullerenes and Related Materials* (eds Kadish, K. M. & Ruoff, R. S.) 1300–1308 (Electrochemical Society, Pennington, 1994).
23. Wagner, C. D., Riggs, W. M., Davis, L. E., Moulder, J. F. & Muilenberg, G. E. (eds) *Handbook of X-ray Photoelectron Spectroscopy* (Perkin-Elmer Corporation, Eden Prairie, Minnesota, 1978).
24. Olmstead, M. M. *et al.* Interaction of curved and flat molecular surfaces. The structures of crystalline compounds composed of fullerene (C_{60}, $C_{60}O$, C_{70}, and $C_{120}O$) and metal octaethylporphyrin units. *J. Am. Chem. Soc.* **121,** 7090–7097 (1999).
25. Anwander, R. *et al.* Synthesis and structural characterization of rare-earth bis(dimethylsilyl)amides and their surface organometallic chemistry on mesoporous MCM-41. *J. Chem. Soc. Dalton Trans.* 847–858 (1998).
26. Dorn, H. C. *et al.* Endohedral metallofullerenes: isolation and characterization. *Proc. Mater. Res. Soc.* **359,** 123–135 (1995).
27. Sheldrich, G. M. Phase Annealing in SHELX: direct methods for larger structures. *Acta Crystallogr. A* **46,** 467–473 (1990).

Supplementary information is available on *Nature*'s World-Wide Web site (http://www.nature.com) or as paper copy from the London editorial office of *Nature*.

Acknowledgements

We thank P. Burbank and Z. Sun for technical support. H.C.D. acknowledges discussions with M. Sherwood, D. S. Bethune, M. Anderson and R. Heflin, and thanks the NSF and the Virginia Tech ASPIRES program for supporting initial phases of this study. A.L.B. thanks the NSF for support.

Correspondence and requests for materials should be addressed to H.C.D. (e-mail: hdorn@chemserver. chem.vt.edu).

A Middle Jurassic mammal from Madagascar

John J. Flynn*, J. Michael Parrish†, Berthe Rakotosamimanana‡, William F. Simpson* & André R. Wyss§

* *Department of Geology, Field Museum of Natural History, Chicago, Illinois 60605, USA*
† *Department of Biological Sciences, Northern Illinois Univeristy, DeKalb, Illinois 60115, USA*
‡ *Département de Paléontologie et Anthropologie Biologique, Université d'Antananarivo, Antananarivo 101, Madagascar*
§ *Department of Geological Sciences, University of California, Santa Barbara, California 93106, USA*

The lower molars of tribosphenic mammals (marsupials, placentals and their extinct allies) are marked, primitively, by a basined heel (talonid) acting as the mortar to the pestle of a large inner cusp (protocone) on the opposing upper teeth. Here we report the earliest tribosphenic mammal found so far, three lower teeth in a jaw fragment from Middle Jurassic (Bathonian, ~167 ± 2 Myr)[1] sediments of northwest Madagascar. This specimen extends the stratigraphic range of the Tribosphenida by some 25 million years, more than doubling the age of the oldest mammal known from Madagascar[2], and representing only the second pre-Plio/Pleistocene terrestrial mammal known from the island. Although it indicates a more ancient diversification of the Triposphenida than previously thought, this find fails to confirm molecular-clock-based models proposing a Middle Jurassic divergence of marsupials and placentals[3]. In addition, it offers a glimpse of mammal evolution on the southern continents during the Middle through Late Jurassic, countering the prevailing view[4] of a northern origin for tribosphenic mammals.

The miniscule mammal reported here is from the youngest of a series of early Mesozoic vertebrate faunas discovered in the Isalo 'Group' of western Madagascar[5]. The locality is in the upper level of the Isalo's tripartite division (Isalo III) in the Mahajanga Basin. It lies near the top of the 'Bathonian Faciès Mixte Dinosauriens' of Isalo IIIb, the age of which is based on a rich invertebrate fauna[6] including the diagnostic echinoids *Nucleolites amplus* and *Acrosalenia colcanapi*. 'Crocodile' and plesiosaur teeth, plus fragmentary remains of the sauropod dinosaur *Lapparentosaurus*

© 1999 Macmillan Magazines Ltd

Immunoprecipitation

For co-precipitation experiments of endogenous proteins, 2×10^7 Rat-1 cells were lysed by sonication in PBS, and the immunoprecipitates were washed 4 times with PBS. Otherwise cells were lysed as described[21]. The antibodies used were crafVI, a peptide antibody against the 12 carboxy-terminal amino acids of Raf-1 (ref. 21); a Raf monoclonal antibody to the regulatory domain (Transduction Laboratories); anti-MEK H8 (Santa Cruz); anti-RKIP raised in rabbits immunized with purified GST–RKIP; anti-HA, 12CA5 monoclonal antibody; monoclonal anti-phospho-ERK (Sigma) and polyclonal anti-phospho-MEK antibodies (New England Biolabs); and anti-GST (Pharmacia).

Kinase assays

These were done as described[21]. For *in vitro* reconstruction of the Raf/MEK/ERK cascade, activated Raf-1 was generated by co-expressing GST–Raf-1 with v-Ras and Lck in Sf-9 cells and collected on glutathione-sepharose beads[21]. Subsequent thrombin cleavage released Raf-1, which was fully active and >90% pure. To activate MEK and ERK *in vitro*, 20 ng of activated Raf-1 was incubated with 40 ng of purified His/MEK-1 and 250 ng of GST–ERK-2 in Raf kinase buffer containing 20 μM ATP for 20 min at 30 °C. To measure kinase activities at individual steps, the respective downstream components were omitted. The activation reactions were diluted into 50 μl Raf kinase buffer[21] containing 20 μM ATP to yield equimolar concentrations of the kinases to be assayed and incubated with increasing amounts of purified RKIP on ice for 10 min. Then, 2 μCi[^{32}P]-γ-ATP and recombinant substrates were added and incubated for 20 min at 30 °C. As substrates, we used 200 ng kinase negative His/MEK-1 for Raf, 1 μg kinase negative GST–ERK for MEK and 1 μg GST–ELK (New England Biolabs) for ERK. In some assays 1 μg GST–MEK was used as the Raf-1 substrate with identical results.

Transfections

COS-1 cells were transfected as described[23] with 2 μg of HA–ERK-2, BXB, MEK and MEK-DD plasmids and the indicated amounts of p353/RKIP. The total amount of transfected DNA was kept constant using the appropriate vectors as carrier DNA. NIH 3T3 and 208F cells were transfected in 6-well plates with 1 μg of pCMV5-BXB and 3 μg of p353/RKIP using Superfect (Qiagen). For RKIP downregulation experiments, NIH 3T3 cells were transiently cotransfected using lipofectamine with 0.5 μg of pHACT[20] and 1.5 or 3 μg RKIP antisense expression vector (pAS-C143) or control vector (pCMVori) as indicated. pHACT expresses a truncated polyoma large-T construct with origin-binding activity, but does not bind Rb or p53, and boosts the expression of pAS-C143 to high levels. In addition, 0.1 μg of an AP1-Luc reporter was transfected for reporter-gene assays. 48 hours after transfection, cells were serum starved for 20 h and either left untreated or treated with TPA (200 ng ml^{-1}) or serum for 5 h before being collected. Cells were lysed and cell extracts were used for immunoblotting or assayed for luciferase activity. For the green fluorescent protein (GFP) sorting experiments, 5×10^6 NIH 3T3 cells were electroporated with either 100 μg pCMVori, 50 μg pCMV–GFP and 50 μg pHACT, or 100 μg pASC143, 50 μg CMV–GFP and 50 μg CMV–HAC. Two days later cells were trypsinized and sorted for green fluorescent cells by preparative FACS. 100,000 GFP-positive cells were lysed in SDS-gel sample buffer and immunoblotted.

Microinjection

Microinjection of antibodies and reporter genes was done as described[24,25]. The RKIP antiserum was purified over a GST–RKIP affinity column. Cells were stained with an activation-specific anti-phospho-ERK monoclonal antibody (New England Biolabs). ERK phosphorylation was quantified by densitometry. For this purpose areas with micro-injected cells were randomly photographed, and the staining intensity of whole individual cells was measured using the PcBAS software.

Received 8 April; accepted 8 July 1999.

1. Ferrell, J. E. Jr MAP kinases in mitogenesis and development. *Curr. Top. Dev. Biol.* **33,** 1–60 (1996).
2. Morrison, D. K. & Cutler, R. E. The complexity of Raf-1 regulation. *Curr. Opin. Cell Biol.* **9,** 174–179 (1997).
3. Moodie, S. A., Willumsen, B. M., Weber, M. J. & Wolfman, A. Complexes of Ras/GTP with Raf-1 and mitogen-activated protein kinase kinase. *Science* **260,** 1658–1661 (1993).
4. Schaeffer, H. J. *et al.* MP1: A MEK binding partner that enhances enzymatic activation of the MAP kinase cascade. *Science* **281,** 1668–1671 (1998).
5. Bruder, J. T., Heidecker, G. & Rapp, U. R. Serum-, TPA-, and Ras-induced expression from Ap-1/Ets-driven promoters requires Raf-1 kinase. *Genes Dev.* **6,** 545–556 (1992).
6. Li, S. *et al.* Regulation of Raf-1 kinase activity by the I4-3-3 family of proteins. *EMBO J.* **14,** 685–696 (1995).
7. Schoentgen, F. & Jolles, P. From structure to function: possible biological roles of a new widespread protein family binding hydrophobic ligands and displaying a nucleotide binding site. *FEBS Lett.* **369,** 22–26 (1995).
8. Kortenjann, M. Thomae, O. & Shaw, P. E. Inhibition of v-raf-dependent c-fos expression and transformation by a kinase-defective mutant of the mitogen-activated protein kinase Erk2. *Mol. Cell. Biol.* **14,** 4815–4824 (1994).
9. Rapp, U. R., Troppmair, J., Beck, T. & Birrer, M. J. Transformation by Raf and other oncogenes renders cells differentially sensitive to growth inhibition by a dominant negative c-jun mutant. *Oncogene* **9,** 3493–3498 (1994).
10. Kolch, W. *et al.* Raf revertant cells resist transformation by non-nuclear oncogenes and are deficient in the induction of early response genes by TPA and serum. *Oncogene* **8,** 361–370 (1993).
11. Catling, A. D., Schaeffer, H. J., Reuter, C. W., Reddy, G. R. & Weber, M. J. A proline-rich sequence unique to MEK1 and MEK2 is required for raf binding and regulates MEK function. *Mol. Cell. Biol.* **15,** 5214–5225 (1995).
12. Kolch, W. *et al.* Inhibition of Raf-1 signaling by a monoclonal antibody, which interferes with Raf-1 activation and with Mek substrate binding. *Oncogene* **13,** 1305–1314 (1996).
13. Hallberg, B., Rayter, S. I. & Downward, J. Interaction of Ras and Raf in intact mammalian cells upon extracellular stimulation. *J. Biol. Chem.* **269,** 3913–3916 (1994).
14. Ferrell, J. E. Jr Tripping the switch fantastic: how a protein kinase cascade can convert graded inputs into switch-like outputs. *Trends Biochem. Sci.* **21,** 460–466 (1996).
15. Tombes, R. M. *et al.* The mitogen-activated protein (MAP) kinase cascade can either stimulate or inhibit DNA synthesis in primary cultures of rat hepatocytes depending upon whether its activation is acute/phasic or chronic. *Biochem. J.* **330,** 1451–1460 (1998).
16. Marshall, C. J. Specificity of receptor tyrosine kinase signaling: transient versus sustained extracellular signal-regulated kinase activation. *Cell* **80,** 179–185 (1995).
17. Sewing, A., Wiseman, B., Lloyd, A. C. & Land, H. High-intensity Raf signal causes cell cycle arrest mediated by p21Cip1. *Mol. Cell. Biol.* **17,** 5588–5597 (1997).
18. Woods, D. *et al.* Raf-induced proliferation or cell cycle arrest is determined by the level of Raf activity with arrest mediated by p21Cip1. *Mol. Cell. Biol.* **17,** 5598–5611 (1997).
19. Grandy, D. K. *et al.* Purificaton, cloning, and tissue distribution of a 23-kDa rat protein isolated by morphine affinity chromatography. *Mol. Endocrinol.* **4,** 1370–1376 (1990).
20. Gjorup, O. V., Rose, P. E., Holman, P. S., Bockus, B. J. & Schaffhausen, B. S. Protein domains connect cell cycle stimulation directly to initiation of DNA replication. *Proc. Natl Acad. Sci. USA* **91,** 12125–12129 (1994).
21. Häfner, S. *et al.* Mechanism of inhibition of Raf-1 by protein kinase A. *Mol. Cell. Biol.* **14,** 6696–6703 (1994).
22. Guan, K. L. & Dixon, J. E. Eucaryotic proteins expressed in *Escherichia coli*: An improved thrombin cleavage and purification procedure of fusion proteins with glutathione S-transferase. *Anal. Biochem.* **192,** 262–267 (1991).
23. Mischak, H. *et al.* Negative regulation of Raf-1 by phosphorylation of serine 621. *Mol. Cell. Biol.* **16,** 5409–5418 (1996).
24. Lavbinsky, R. M. *et al.* Diverse signaling pathways modulate nuclear receptor recruitment of N-CoR and SMRT complexes. *Proc. Natl Acad. Sci. USA* **95,** 2920–2925 (1998).
25. Rose, D. W., McCabe, G., Feramisco, J. R. & Adler, M. Expression of c-fos and AP-1 activity in senescent human fibroblasts is not sufficient for DNA synthesis. *J. Cell Biol.* **119,** 1405–1411 (1992).
26. Minden, A. *et al.* Differential activation of ERK and JNK mitogen-activated protein kinases by Raf-1 and MEKK. *Science* **266,** 1719–1723 (1994).

Acknowledgements

We thank M. Karin, M. Weber, F. Hofer, P. Shaw, M. Baccarini and B. Schaffhausen for various expression plasmids; D. K. Grandy for the full-length rat cDNA homologue of RKIP; and L. Black for help with microinjections. We appreciate critical reading and helpful comments by members of the Beatson laboratories. This work was in part supported by grants of the AICR, DFG and the Sanders Stiftung to W.K. and H.M. and by an NIH grant to J.M.S.

Correspondence and requests for materials should be addressed to W.K. (e-mail: wkolch@beatson.gla. ac.uk) or J.M.S. (e-mail: john_sedivy@brown.edu).

Saccharomyces cerevisiae telomerase is an Sm small nuclear ribonucleoprotein particle

Anita G. Seto*, Arthur J. Zaug*, Suzanne G. Sobel†, Sandra L. Wolin† & Thomas R. Cech*

** Department of Chemistry and Biochemistry and Howard Hughes Medical Institute, University of Colorado, Boulder, Colorado 80309-0215, USA*
† Department of Cell Biology and Howard Hughes Medical Institute, Yale University School of Medicine, New Haven, Connecticut 06510, USA

Activation of the chromosome end-replicating enzyme telomerase can greatly extend the lifespan of normal human cells[1] and is associated with most human cancers[2]. In all eukaryotes examined, telomerase has an RNA subunit[3], a conserved reverse transcriptase subunit[4] and additional proteins[5,6], but little is known about the assembly of these components. Here we show that the *Saccharomyces cerevisiae* telomerase RNA[7] has a 5′-2,2,7-trimethylguanosine (TMG) cap and a binding site for the Sm proteins, both hallmarks of small nuclear ribonucleoprotein particles (snRNPs) that are involved in nuclear messenger RNA splicing[8,9]. Immunoprecipitation of telomerase from yeast extracts shows that Sm proteins are assembled on the RNA and that most or all of the telomerase activity is associated with the Sm-containing complex. These data support a model in which telomerase RNA is transcribed by RNA polymerase II (ref. 10) and 7-methylguanosine-capped,

© 1999 Macmillan Magazines Ltd

binds the seven Sm proteins, becomes TMG-capped and picks up the other protein subunits. We conclude that the functions of snRNPs assembled by this pathway are not restricted to RNA processing, but also include chromosome telomere replication.

The nature of the 5′ end of an RNA often provides a clue to its biogenesis pathway. The presence of a 5′-TMG cap on telomerase RNA (*TLC1*) was tested by immunoprecipitation of yeast total cellular RNA with anti-TMG antibodies. Northern blot hybridization (Fig. 1) showed that *TLC1* RNA was immunoprecipitated, as was U1 snRNA, which is known to have a TMG cap[11] (32% and 55%, respectively, of the input RNA were bound to the antibody). In contrast, uncapped 5.8S ribosomal RNA was recovered predominantly in the supernatant (only 3.4% bound), providing evidence for the specificity of the immunoprecipitation. Immunoprecipitated RNA from a strain carrying a deletion of the gene for telomerase RNA (*tlc1Δ*) contained U1 and 5.8S RNAs but not *TLC1* RNA, as expected. Yeast telomerase RNA consists of a major poly(A)$^-$ species and a short-lived poly(A)$^+$ transcript that is thought to be its precursor[10]; the poly(A)$^-$ fraction of the telomerase RNA was preferentially enriched on the anti-TMG beads relative to the poly(A)$^+$ fraction (data not shown).

The presence of a TMG cap provided the impetus for searching for additional snRNP features of telomerase RNA. Inspection of the primary sequence of *TLC1* revealed a sequence matching that of the known consensus for Sm protein binding ($AU_{5-6}GPu$) and identical to the Sm site in yeast U4 snRNA[12]. This sequence is near the 3′ end of *TLC1* RNA, similar to its location in other yeast Sm snRNAs (Fig. 2a). To test the functional significance of this putative Sm site, low-copy-number plasmids carrying various mutations in *TLC1* were constructed and individually transformed into a *tlc1Δ rad52*$^-$-strain (Fig. 2a). Disruption of *RAD52* disables the recombination pathway, an alternative mechanism for telomere maintenance in yeast[6], thereby enabling clear assessment of defects in telomerase activity.

Yeast strains with the *tlc1-Sm*$^-$ mutation, which replaces the putative Sm site with an unrelated sequence, or two less severe mutations, *tlc1-Sm2T* and *tlc1-Sm4C5C*, had markedly decreased levels of telomerase RNA (Fig. A in Supplementary Information). The deadenylated mature form was not visible by northern blot analysis. The residual telomerase RNA was the minor polyadenylated species, as shown by its enrichment on an oligo(dT) cellulose column (Fig. 2b). The *tlc1-Sm*$^-$ strain showed a biphasic growth pattern on plates: formation of normal-sized colonies was greatly reduced after about 100–125 generations (compared with 75–100 generations for senescence of the *tlc1Δ* strain), but the cells later recovered and grew normally (Fig. 2a). *Tlc1-Sm2T* and *tlc1-Sm4C5C* showed no growth phenotype. Presumably the residual levels of the mutant telomerase RNAs were sufficient to support cell growth.

Telomere length is often more sensitive to alterations in telomerase function than is cell growth[13]. Southern blot analysis (Fig. 2c) of DNA from the *tlc1-Sm*$^-$ strain showed that the telomeres initially began to shorten and then were maintained at a length shorter than wild-type. This pattern of telomere shortening correlated with the observed growth phenotype and differed from that of the *tlc1Δ* strain, in which the telomeres continued to shorten over time until the cells stopped growing (after the fourth successive culture, see Fig. 2d). In *tlc1-Sm2T* and *tlc1-Sm4C5C*, the telomeres were shorter than wild-type and appeared to remain about the same length, perhaps with very gradual shortening over time. Mutant telomerase RNA levels remained barely detectable over the time-course of this experiment (see Supplementary Information, Fig. A). These results indicate that the Sm proteins may be involved in the stability and function of telomerase RNA.

To test for interaction between Sm proteins and telomerase, we used co-immunoprecipitation experiments. We constructed a strain in which the endogenous *SMD1* gene, encoding one of the core Sm proteins, was replaced with an allele containing an influenza haemagglutinin (HA) epitope tag at its carboxy terminus. This variant of *SMD1* had been previously characterized as a fully functional allele with no overt phenotype when expressed from a low-copy-number plasmid[14]. This strain also carries a gene for the catalytic subunit of yeast telomerase, Est2p, with an amino-terminal Protein A tag integrated at its chromosomal locus. The tag has no significant effect on growth or telomerase function (K. L. Friedman and T.R.C., unpublished data). Extract prepared from this strain was immunoprecipitated for HA–Smd1p with an anti-HA antibody bound to Protein G–agarose beads. Northern blot analysis of RNA extracted from the beads (Fig. 3a) revealed that telomerase RNA co-immunoprecipitated with HA–Smd1p more efficiently than U1 snRNA, previously shown to associate with Sm proteins[15,16]. (Percentages of input RNA bound were 12% and 5%, respectively.) U3 small nucleolar RNA, not known to bind Sm proteins[11], did not co-immunoprecipitate with HA–Smd1p (only 0.09% bound). When extract was prepared from either a wild-type strain or a strain expressing only ProA-Est2p, no appreciable telomerase RNA or U1 snRNA bound to the anti-HA beads, demonstrating the specificity of the co-immunoprecipitation for HA-tagged Smd1p (Fig. 3a).

A second yeast Sm protein, Smd3p, when HA-tagged and expressed from a low-copy-number plasmid[14], also co-immunoprecipitated *TLC1* RNA (data not shown). Additionally, when expression of Smd1 protein was turned off in a strain in which transcription of *SMD1* is controlled by the galactose promoter[14], telomerase RNA levels decreased over time with kinetics similar to those of U1 snRNA, whereas U6, a non-Sm-containing snRNA, was unaffected (see Supplementary Information, Fig. B). Collectively, these data indicate that the Smd1 and Smd3 proteins are physically associated with the telomerase RNA and are required for its accumulation.

To determine whether the *TLC1* RNA associated with Smd1p was part of a functional enzyme, the complex bound to anti-HA beads was assayed *in vitro* for telomerase activity. Upon incubation with a single-stranded telomeric oligonucleotide, dTTP, and [α^{32}P]dGTP, the pattern of extension products characteristic of yeast telomerase[4,17,18] was detected (Fig. 3b, lane 1). This activity was sensitive to treatment with RNase A, a diagnostic property of telomerase (data not shown). The supernatant from the first incubation still contained some residual telomerase activity that was reduced by successive passages over anti-HA beads (Fig. 3b, lanes 2 and 3). Immunoprecipitation of wild-type extract, lacking tagged proteins, gave no detectable telomerase activity (data not shown). In addition, HA immunoprecipitates of extracts made from a strain of yeast carrying a low-copy plasmid encoding HA-tagged Smd3p[14] also contained active telomerase (data not shown). Therefore, yeast telomerase associated with two different Sm proteins has enzymatic activity.

It remained possible that there were two populations of active telomerase, one with and one without the Sm proteins. To test this

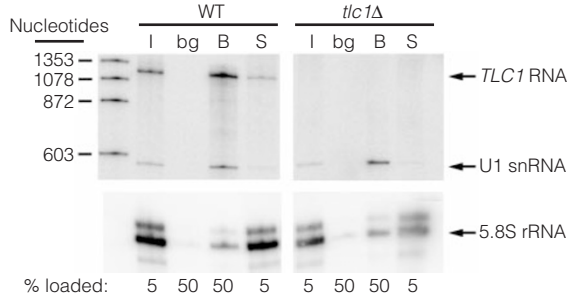

Figure 1 Identification of 5′-TMG cap on telomerase RNA. Northern blot of RNA fractions immunoprecipitated with agarose bead-immobilized anti-TMG antibodies: Input RNA (I), RNA bound to beads lacking antibody (bg), RNA bound to anti-TMG beads (B) and supernatant RNA (S). RNA was prepared from a wild-type (WT) strain and a strain deleted for *TLC1* (*tlc1Δ*), and probed with a random-primed [^{32}P]dCTP-labelled DNA copy of the *TLC1* gene and ^{32}P 5′-end-labelled oligonucleotides complementary to U1 and 5.8S. % loaded is the percentage of the total RNA from each experiment loaded in that lane. Markers in the left-most lane are end-labelled denatured ϕX174 DNA *Hae*III fragments.

© 1999 Macmillan Magazines Ltd

possibility, Smd1p–containing complexes were significantly depleted from extracts of the strain containing both HA-tagged Smd1p and ProA-tagged Est2p by three rounds of incubation with anti-HA beads. The supernatant largely depleted of Smd1p was then incubated with IgG beads (which bind ProA–Est2p) to pull down any remaining telomerase complex, and the beads were assayed for telomerase activity (Fig. 3c, lane 2). In a parallel immunoprecipitation, an identical extract was treated with three rounds of control agarose beads; telomerase was then bound to IgG beads that were assayed for activity (Fig. 3c, lane 1). Quantification showed that the fraction of active telomerase containing the Sm protein is at least 77 ± 7% (average ± range of four experiments; given the incomplete nature of immunodepletion, this is a minimum estimate). These values were corrected for the small amount of telomerase activity lost nonspecifically on the anti-HA beads, as determined by preparing extract from a strain expressing only ProA–Est2p and subjecting it to three rounds of depletion by anti-HA or control beads followed by binding to IgG beads (Fig. 3c, lanes 3 and 4). An additional control showed that telomerase activity from wild-type extracts was not bound to IgG beads (Fig. 3c, lanes 5 and 6). Western blot analysis revealed a reduction in Est2p after immunoprecipitation of the Smd1p-containing complex from the doubly-tagged strain (see Supplementary Information, Fig. C). These results indicate that at least the majority of telomerase in yeast is associated with Smd1p.

We have shown that the yeast telomerase RNA shares two key characteristics of the splicing snRNAs: capping by 5′-TMG and association with Sm proteins. Additionally, telomerase RNA has a polyadenylated species that is processed to a mature form[10]; minor polyadenylated fractions of U1 and U2 snRNAs have also been reported[19,20]. To our knowledge, yeast telomerase is the only Sm-containing snRNP whose known function is not RNA processing,

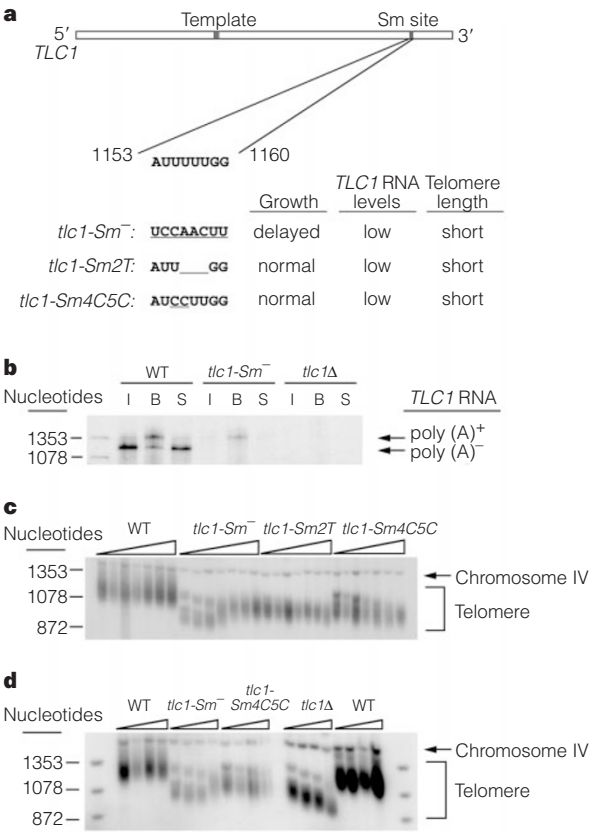

Figure 2 Characterization of mutants in the putative Sm protein binding site. **a**, The putative Sm site in *TLC1* RNA, mutations and deletions introduced in the site (underlined bases) and summary of observed phenotypes. **b**, *TLC1* RNA levels in Sm mutants were lower than wild-type and the remaining RNA was enriched on oligo(dT) cellulose. Northern blot of input (I), bound (B) and supernatant (S) fractions from oligo(dT) chromatography probed with *TLC1* gene probe. **c**, Telomere lengths of Sm site mutants were shorter than wild-type. Southern blot of genomic DNA digested with *Xho*I, hybridized with random-primed [^{32}P]dCTP-labelled DNA copies of telomeric sequence and a region in chromosome IV. *Xho*I cuts internal to the telomere in chromosomes containing Y′ elements, producing a diffuse band of ~1–1.3 kilobases. Triangular wedges represent ~10–90 generations from seven successive cultures. The chromosome IV signal served as an internal loading control as well as a marker for measuring relative telomere lengths. **d**, Telomere shortening in Sm site mutants was not as severe as in the *tlc1Δ* strain. DNA was extracted from four successive cultures, ~10–50 generations. The *tlc1Δ* strain did not grow past the fourth culture. Wild-type DNA on the left was grown and prepared in parallel with *tlc1-Sm⁻* and *tlc1-Sm4C5C* DNA; wild-type on the right was from the same experiment as *tlc1Δ*.

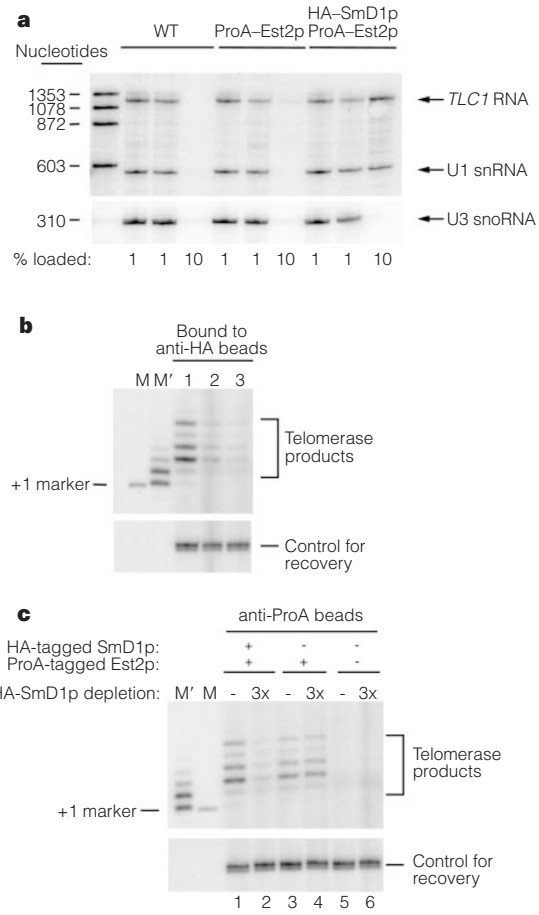

Figure 3 HA-tagged Smd1 protein co-immunoprecipitates *TLC1* RNA and *in vitro* telomerase activity. **a**, Co-immunoprecipitation of *TLC1* RNA with HA–Smd1p. Extract was prepared from a wild-type (WT) strain, a singly tagged strain expressing only ProA–Est2p, or a doubly tagged strain expressing both ProA–Est2p and HA–Smd1p. RNA that co-immunoprecipitated on anti-HA antibody beads from these strains was analysed by northern blot and probed with the *TLC1* gene probe and U1 and U3 oligonucleotide probes. I, input RNA; S, RNA in supernatant; B, RNA bound to beads. **b**, Co-immunoprecipitation of telomerase activity with HA–Smd1p. Extract prepared from a strain expressing HA-tagged Smd1p and ProA–Est2p was incubated with anti-HA antibody beads and the complexes on the beads were assayed for *in vitro* telomerase activity. Lane 1, telomerase activity precipitated on anti-HA beads; lanes 2 and 3, activity precipitated on a second and third passage of anti-HA beads, respectively. Control for recovery was a ^{32}P 5′-end-labelled 100-mer oligo added immediately after the reactions were stopped and visualized on the same gel. As markers, the 14-mer single-stranded telomeric primer was extended by one nucleotide with the addition of [^{33}P]ddTTP (M) or converted to a ladder with [^{32}P]dTTP and terminal transferase (M′). **c**, Most of the active telomerase contains Smd1p. Extracts prepared from strains described in **a** were incubated with three sequential batches of anti-HA beads (3×) or control beads lacking anti-HA antibody (–). The supernatants from these immunoprecipitations were then incubated with IgG beads to bind ProA–Est2p, thereby collecting the remaining telomerase activity. IgG beads were assayed for *in vitro* telomerase activity.

© 1999 Macmillan Magazines Ltd

but rather DNA replication. The telomerase complex containing the Sm proteins has *in vitro* telomerase activity and represents the majority of telomerase activity in extracts. We infer that the Sm proteins constitute seven new telomerase subunits; we have provided direct evidence only for D1 and D3, but their participation in a ring of no less than seven subunits[21] makes it likely that the other five are also present in telomerase.

The human telomerase RNA also has a TMG cap but the RNA is not detected by northern analysis in anti-Sm immunoprecipitates (A.J.Z., S.L.W. and T.R.C., data not shown; S. Lichtsteiner and S. L. Weinrich, personal communication), although it remains possible that the Sm epitope is masked in a large complex. The human RNA has a 3′ domain characteristic of small nucleolar RNPs[22]. Therefore, it remains to be seen whether the biogenesis of the human telomerase is different or shares features with the yeast enzyme.

We propose a model for the biogenesis of yeast telomerase. The RNA subunit is transcribed by RNA polymerase II accompanied by 7-methyl G capping and polyadenylation[10]. The poly(A) tail is then removed by 3′-processing, which appears to require Sm protein binding, as shown by the fact that the poly(A)$^+$ subfraction accumulates in the Sm-site RNA mutants. Binding of the Sm proteins to the Sm site also promotes the hypermethylation of the 5′ cap to a trimethyl-G. In vertebrates, the U1, U2, U4 and U5 snRNAs are exported to the cytoplasm, where they bind Sm proteins, gain a TMG cap and are then re-imported into the nucleus[23]. If such a cytoplasmic phase of the pathway occurs in yeast, it might provide an advantageous location for assembly of the telomerase complex, as the catalytic subunit (Est2p) and other telomerase proteins (such as Est1p[24] and Est3p[6,13]) are synthesized in the cytoplasm. However, because shuttling of snRNAs between the nucleus and cytoplasm has not been shown in budding yeast, the yeast telomerase could be assembled entirely in the nucleus, where it ultimately functions. □

Methods

S. cerevisiae strains and manipulations

Strain TCy43 (*Δtlc1::LEU2*, *rad52::LEU2*, pl-TLC1$^+$-LYS2$^+$-CEN) was transformed with either pSD107 [*CEN*, *TRP1*, *TLC1*], pAS500 [*CEN*, *TRP1*, *tlc1Δ*], pAS501 [*CEN*, *TRP1*, *tlc1-sm*$^-$], pAS502 [*CEN*, *TRP1*, *tlc1-sm2T*] or pAS503 [*CEN*, *TRP1*, *tlc1-sm4C5C*], and then grown on α-aminoadipate to counterselect plasmid pl-TLC1$^+$-LYS2$^+$-CEN as described[25,26]. The construct for the integration of the haemagglutinin epitope tag into the *SMD1* locus was made by ligating PCR fragments corresponding to nucleotides 55–452 of the *SMD1* open reading frame of plasmid pGAL::SMD1HA[14] and nucleotides 447–907 of the downstream flanking region of *SMD1* (amplified from TVL268, see below) into plasmid pRS306. The correct sequence of the entire region was confirmed with automated sequencing. Integration of *HA–SMD1* was performed by the pop-in/pop-out method[27] into the wild-type strain TVL268 (V. Lundblad) and into YKF103 (details of strain construction to be described elsewhere; K. L. Friedman and T.R.C., unpublished data). Correct integration was confirmed by PCR. For additional strain information and plasmid construction, see Methods in Supplementary Information.

TMG immunoprecipitations and poly(A)$^+$ isolation of RNA

See Methods in Supplementary Information.

Measurements of telomere length

See Methods in Supplementary Information.

Co-immunoprecipitation experiments

Yeast cultures were grown to 0.9–1.5 OD (600 nm). Extracts were prepared by a glass-bead lysis method in PMG-150 (10 mM phosphate pH 6.8, 1 mM $MgCl_2$, 10% glycerol, 150 mM NaCl, 1 mM DTT, 0.1 mM EDTA, 1 mM PMSF, 1 U μl^{-1} RNasin (Promega)). The low salt, low pH buffer was used to decrease the affinity of the Protein A tag to the anti-HA antibody (mouse IgG_1)[28]. For HA immunoprecipitation, anti-HA antibody beads were prepared by overnight incubation of 250–350 μg of monoclonal antibody HA.11 (Babco) to 200 μl of packed protein G Plus-Agarose (Oncogene). Beads were washed extensively with PBS. To 1.5–2.5 mg of whole cell extract, 20 μl of packed anti-HA-beads was added. After binding for 4–12 h, the beads were washed extensively with PMG-150. ProA–Est2p immunoprecipitations were performed by incubation of 1.5–2.5 mg extract with IgG Sepharose beads (Amersham Pharmacia) for 12 h. RNA associated with the antibody–antigen complexes on the anti-HA or IgG beads was isolated as described[14]. RNA was isolated from extract by treatment with 0.4 mg ml^{-1} proteinase K for 15 min at 37 °C followed by phenol/chloroform extraction and precipitation with 0.3 M NaOAc and 3 volumes cold 100% EtOH. RNA was then analysed by northern blot as described[10].

Telomerase activity assay.

Telomerase complex bound to 5 μL packed HA or IgG beads was incubated in telomerase assay buffer (40 mM Tris-HCl, pH 7.5, 50 mM NaCl, 5% glycerol, 0.5 mM spermidine, 0.5 mM DTT, 2.5 μM substrate oligo (5′-GTGTGGTGTGTGGG-3′), 100 μM dTTP, 1.70 μM [α^{32}P]dGTP) for 20 min at 30 °C. Alternatively, reactions were performed with 100 μM ddGTP and 1.70 μM [α^{32}P]dTTP (data not shown). To the reaction, ^{32}P-5′-end-labelled 100-mer was added as a loading control along with 1 μl glycogen. Products were phenol/chloroform extracted, then ethanol precipitated with 7.5 M NH_4OAc and 2.5 volumes cold 100% ethanol. Products were resolved on a 12% PAGE–urea sequencing gel and visualized with a Molecular Dynamics PhosphorImager.

Received 26 April; accepted 15 July 1999.

1. Bodnar, A. G. *et al.* Extension of life-span by introduction of telomerase into normal human cells. *Science* **279,** 349–352 (1998).
2. Kim, N. W. *et al.* Specific association of human telomerase activity with immortal cells and cancer. *Science* **266,** 2011–2103 (1994).
3. Greider, C. W. & Blackburn, E. H. A telomeric sequence in the RNA of *Tetrahymena* telomerase required for telomere repeat synthesis. *Nature* **337,** 331–337 (1989).
4. Lingner, J. *et al.* Reverse transcriptase motifs in the catalytic subunit of telomerase. *Science* **276,** 561–567 (1997).
5. Bryan, T. M. & Cech, T. R. Telomerase and the maintenance of chromosome ends. *Curr. Opin. Cell Biol.* **11,** 318–324 (1999).
6. Nugent, C. I. & Lundblad, V. The telomerase reverse transcriptase: components and regulation. *Genes Dev.* **12,** 1073–1085 (1998).
7. Singer, M. S. & Gottschling, D. E. TLC1: template RNA component of *Saccharomyces cerevisiae* telomerase. *Science* **266,** 404–409 (1994).
8. Lührmann, R., Kastner, B. & Bach, M. Structure of spliceosomal snRNPs and their role in pre-mRNA splicing. *Biochim. Biophys. Acta* **1087,** 265–292 (1990).
9. Mattaj, I. W. Cap trimethylation of U snRNA is cytoplasmic and dependent on U snRNP protein binding. *Cell* **46,** 905–911 (1986).
10. Chapon, C., Cech, T. R. & Zaug, A. J. Polyadenylation of telomerase RNA in budding yeast. *RNA* **3,** 1337–1351 (1997).
11. Yu, Y.-T., Scharl, E. C., Smith, C. M. & Steitz, J. A. in *The RNA World* (eds Gesteland, R. F., Cech, T. R. & Atkins, J. F.) 487–524 (Cold Spring Harbor Lab. Press, Cold Spring Harbor, New York, 1999).
12. Jones, M. H. & Guthrie, C. Unexpected flexibility in an evolutionarily conserved protein–RNA interaction: genetic analysis of the Sm binding site. *EMBO J.* **9,** 2555–2561 (1990).
13. Lendvay, T. S., Morris, D. K., Sah, J., Balasubramanian, B. & Lundblad, V. Senescence mutants of *Saccharomyces cerevisiae* with a defect in telomere replication identify three additional EST genes. *Genetics* **144,** 1399–1412 (1996).
14. Roy, J., Zheng, B., Rymond, B. C. & Woolford, J. L. Jr Structurally related but functionally distinct yeast Sm D core small nuclear ribonucleoprotein particle proteins. *Mol. Cell. Biol.* **15,** 445–455 (1995).
15. Pettersson, I., Hinterberger, M., Mimori, T., Gottlieb, E. & Steitz, J. A. The structure of mammalian small nuclear ribonucleoproteins: identification of multiple protein components reactive with anti-(U1)RNP and anti-Sm autoantibodies. *J. Biol. Chem.* **259,** 5907–5914 (1984).
16. Neubauer G. *et al.* Identification of the proteins of the yeast U1 small nuclear ribonucleoprotein complex by mass spectrometry. *Proc. Natl Acad. Sci. USA* **94,** 385–390 (1997).
17. Cohn, M. & Blackburn, E. H. Telomerase in yeast. *Science* **269,** 396–400 (1995).
18. Prescott, J. & Blackburn, E. H. Telomerase RNA mutations in *Saccharomyces cerevisiae* alter telomerase action and reveal nonprocessivity *in vivo* and *in vitro*. *Genes Dev.* **11,** 528–540 (1997).
19. Seipelt, R. L., Zhang, B., Asuru, A. & Rymond, B. U1 snRNA is cleaved by RNase III and processed through an Sm site-dependent pathway. *Nucleic Acids Res.* **27,** 587–595 (1999).
20. Elela, S. A. & Ares, M. Jr Depletion of yeast RNase III blocks correct U2 3′ end formation and results in polyadenylated but functional U2 snRNA. *EMBO J.* **17,** 3738–3746 (1998).
21. Kambach, C. *et al.* Crystal structures of two Sm protein complexes and their implications for the assembly of the spliceosomal snRNPs. *Cell* **96,** 375–387 (1999).
22. Mitchell, J. R., Cheng, J. & Collins, K. A box H/ACA small nucleolar RNA-like domain at the human telomerase RNA 3′ end. *Mol. Cell. Biol.* **19,** 567–576 (1999).
23. Mattaj, I. W. in *Structure and Function of Major and Minor Small Nuclear Ribonucleoprotein Particles* (ed. Birnstiel, M. L.) 100–114 (Springer, Berlin, 1988).
24. Virta-Pearlman, G., Morris, D. K. & Lundblad, V. Est1 has the properties of a single-stranded telomere end-binding protein. *Genes Dev.* **10,** 3094–3104 (1996).
25. Rose, M. D., Winston, F. & Hieter, P. *Methods in Yeast Genetics. A Laboratory Manual* 177–186 (Cold Spring Harbor Lab. Press, Cold Spring Harbor, New York, 1990).
26. Schiestl, R. H. & Gietz, R. D. High efficiency transformation of intact yeast cells using single stranded nucleic acids as a carrier. *Curr. Genet.* **16,** 339–346 (1989).
27. Scherer, S. & Davis, R. W. Replacement of chromosome segments with altered DNA sequences constructed *in vitro*. *Proc. Natl Acad. Sci. USA* **76,** 4951–4955 (1979).
28. Ey, P. L., Prowse, S. J. & Jenkin, C. R. Isolation of pure IgG1, IgG2a and IgG2b immunoglobins from mouse serum using Protein A-sepharose. *Immunochemistry* **15,** 429–436 (1978).

Supplementary information is available on *Nature*'s World-Wide Web site (http://www.nature.com) as paper copy from the London editorial offices of *Nature*.

Acknowledgements

We thank K. Friedman, D. Gottschling, and B. Rymond for yeast plasmids and strains; R. Weilbaecher and V. Lundblad for their telomerase activity assay protocol; and the Cech lab and J. Goodrich for discussions. This work was supported by grants from the NIH to T.R.C. and S.L.W. T.R.C. and S.L.W. are investigators of the Howard Hughes Medical Institute.

Correspondence and requests for material should be addressed to T.R.C. (e-mail: thomas.cech@colorado. edu).

© 1999 Macmillan Magazines Ltd

direction of cardiac looping. The similarity of the cardiac and pulmonary phenotypes of *Pitx2*$^{-/-}$ and *ActRIIB*$^{-/-}$ (ref. 17) indicates that Pitx2 is the critical downstream target of ActRIIB, a putative Nodal receptor, mediating effects on both cardiac positioning and pulmonary isomerism. The *Pitx2* phenotype extends to tissues other than those affected by *ActRIIB*, indicating that *Pitx2* gene activation may be controlled separately in these tissues. Pitx2 is thus, to our knowledge, the first transcription factor that can be considered to be a critical component in mediating the proliferative/motility events of the lateral-plate mesoderm that underlie ventral body-wall closure and 'leftness' in lung patterning and organ placement, as well as serving critical later roles in organogenesis. □

Methods

Generation of *Pitx2*-knockout mice.

Genomic clones encompassing the entire *Pitx2* transcript were obtained from the 129/SvJ mouse genomic library (Stratagene). The 5′-arm is a 5.0-kilobase (kb) *Nde*I–*Ngo*MI fragment bordering the DNA-binding domain and the 3′-arm is a 4.5-kb *Bam*HI–*Sal*I 3′-end fragment that includes the entire 3′ untranslated region. The region from the homeodomain to the C-terminus of *Pitx2* is replaced by the *LacZ/neomycin* sequences, driven by the *Pitx2* promoter. R1 embryonic stem cells were grown and selected with G418 and gancyclovir, and Southern blot analysis was carried out using a 5′-external (1.6-kb) probe that hybridizes to a 8-kb *Kpn*I wild-type and a 6-kb *Kpn*I/*Bam*HI recombinant band. We confirmed genotyping of heterozygotes and homozygotes using a 3′-internal (0.6-kb) probe that recognizes a 3.6-kb *Pst*I fragment in the wild-type and a 2.8-kb *Pst*I fragment in the recombinant alleles.

In situ hybridization, whole-mount hybridization and *LacZ* staining.

Isolation, fixation, and hybridization with ^{35}S-labelled antisense RNA probes and exposure were done as described[1]. For whole-mount *in situ* hybridization studies, embryos were briefly fixed in 4% paraformaldehyde followed by methanol and hydrogen peroxide washes and proteinase-K treatment as described[1]. All probes were as described[1,2], or derived by PCR and sequenced.

Received 4 May; accepted 13 July 1999.

1. Szeto, D. P. *et al.* Role of the Bicoid-related homeodomain factor Pitx1 in specifying hindlimb morphogenesis and pituitary development. *Genes Dev.* **13,** 484–494 (1999).
2. Logan, M. & Tabin, C. J. Role of Pitx1 upstream of Tbx4 in specification of hindlimb identity. *Science* **283,** 1736–1739 (1999).
3. Lanctot, C., Lamolet, B. & Drouin, J. The bicoid-related homeoprotein Ptx1 defines the most anterior domain of the embryo and differentiates posterior from anterior lateral mesoderm. *Development* **124,** 2807–2817 (1997).
4. Semina, E. V. *et al.* Cloning and characterization of a novel bicoid-related homeobox transcription factor gene, RIEG, involved in Rieger syndrome. *Nature Genet.* **14,** 392–399 (1996).
5. Gage, P. J. & Camper, S. A. Pituitary homeobox 2, a novel member of the bicoid-related family of homeobox genes, is a potential regulator of anterior structure formation. *Hum. Mol. Genet.* **6,** 457–464 (1997).
6. Campione, M. *et al.* The homeobox gene Pitx2: mediator of asymmetric left-right signaling in vertebrate heart and gut looping. *Development* **126,** 1225–1234 (1999).
7. Piedra, M. E., Icardo, J. M., Albajar, M., Rodriguez-Rey, J. C. & Ros, M. A. Pitx2 participates in the late phase of the pathway controlling left-right asymmetry. *Cell* **94,** 319–324 (1998).
8. Logan, M., Pagan-Westphal, S. M., Smith, D. M., Paganessi, L. & Tabin, C. J. The transcription factor Pitx2 mediates situs-specific morphogenesis in response to left-right asymmetric signals. *Cell* **94,** 307–317 (1998).
9. Yoshioka, H. *et al.* Pitx2, a bicoid-type homeobox gene, is involved in a lefty-signaling pathway in determination of left-right asymmetry. *Cell* **94,** 299–305 (1998).
10. Meno, C. *et al.* lefty-1 is required for left-right determination as a regulator of lefty-2 and nodal. *Cell* **94,** 287–297 (1998).
11. Ryan, A. K. *et al.* Pitx2 determines left-right asymmetry of internal organs in vertebrates. *Nature* **394,** 545–551 (1998).
12. Mucchielli, M. L. *et al.* Mouse Otlx2/RIEG expression in the odontogenic epithelium precedes tooth initiation and requires mesenchyme-derived signals for its maintenance. *Dev. Biol.* **189,** 275–284 (1997).
13. Semina, E. V., Reiter, R. S. & Murray, J. C. Isolation of a new homeobox gene belonging to the Pitx/Rieg family: expression during lens development and mapping to the aphakia region on mouse chromosome 19. *Hum. Mol. Genet.* **6,** 2109–2116 (1997).
14. Thomas, T., Yamagishi, H., Overbeek, P. A., Olson, E. N. & Srivastava, D. The bHLH factors, dHAND and e HAND, specify pulmonary and systemic cardiac ventricles independent of left-right sidedness. *Dev. Biol.* **196,** 228–236 (1998).
15. Biben, C. & Harvey, R. P. Homeodomain factor Nkx2-5 controls left/right asymmetric expression of bHLH gene eHand during murine heart development. *Genes Dev.* **11,** 1357–1369 (1997).
16. Hogan, B. L. Morphogenesis. *Cell* **96,** 225–233 (1999).
17. Oh, S. P. & Li, E. The signaling pathway mediated by the type IIB activin receptor controls axial patterning and lateral asymmetry in the mouse. *Genes Dev.* **11,** 1812–1826 (1997).
18. Ericson, J., Norlin, S., Jessell, T. M. & Edlund, T. Integrated FGF and BMP signaling controls the progression of progenitor cell differentiation and the emergence of pattern in the embryonic anterior pituitary. *Development* **125,** 1005–1015 (1998).
19. Treier, M. *et al.* Multistep signaling requirements for pituitary organogenesis in vivo. *Genes Dev.* **12,** 1691–1704 (1998).
20. Dasen, J. S. *et al.* Reciprocal interactions of Pit-1 and GATA-2 mediate signaling gradient-induced determination of pituitary cell types. *Cell* **97,** 1–20 (1999).
21. Sheng, H. Z. *et al.* Multistep control of pituitary organogenesis. *Science* **278,** 1809–1812 (1997).
22. Peters, H. & Balling, R. Teeth. Where and how to make them. *Trends Genet.* **15,** 59–65 (1999).
23. Martinez, S., Crossley, P. H., Cobos, I., Rubenstein, J. L. & Martin, G. R. FGF8 induces formation of an ectopic isthmic organizer and isthmocerebellar development via a repressive effect on otx2 expression. *Development* **126,** 1189–1200 (1999).
24. Boettger, T., Whittler, L. & Kessel, M. FGF8 functions in the specification of the right body side of the chick. *Curr. Biol.* **9,** 277–280 (1999).
25. Collignon, J., Varlet, I. & Robertson, E. J. Relationship between asymmetric nodal expression and the direction of embryonic turning. *Nature* **381,** 155–158 (1996).
26. Lowe, L. A. *et al.* Conserved left-right asymmetry of nodal expression and alterations in murine *situs inversus*. *Nature* **381,** 158–161 (1996).

Acknowledgements

We thank E. Olson, B. Hogan, G. Martin, P. Sharp and P. Overbeek for helpful discussions; M. Treier, A. Gleiberman, R. Burgess, A Ryan and other members of the laboratory for critical advice, data and discussion; E. Olson, B. Hogan, and P. Gruss for critical reagents; M. Ayers for animal handling; P. Myer for her expertise in preparation of illustrations; and M. Fisher for manuscript preparation. P.B. is on leave from the Advanced Biotechnology Center/IST Genoa, Italy, and is supported by the American Italian Cancer Foundation (Bristol-Myers Squibb Foundation). M.G.R. is an Investigator with the Howard Hughes Medical Institute. This work is supported by NIH grants to M.G.R. and J.C.I.B., and the G. Harold and Leila Y. Mathers Charitable Foundation to J.C.I.B.

Correspondence and requests for materials should be addressed to M.G.R. (e-mail: mrosenfeld@ ucsd.edu) or J.C.I.-B. (e-mail: belmonte@salk.edu).

Human urotensin-II is a potent vasoconstrictor and agonist for the orphan receptor GPR14

Robert S. Ames*†, Henry M. Sarau†‡, Johathan K. Chambers§, Robert N. Willette‡, Nambi V. Aiyar‡, Anne M. Romanic‡, Calvert S. Louden‖, James J. Foley‡, Charles F. Sauermelch‡, Robert W. Coatney¶, Zhaohui Ao‡, Jyoti Disa‡, Stephen D. Holmes#, Jeffrey M. Stadel‡, John D. Martin☆, Wu-Schyong Liu☆, George I. Glover☆, Shelagh Wilson§, Dean E. McNulty☆, Catherine E. Ellis*, Nabil A. Elshourbagy*, Usman Shabon*, John J. Trill, Douglas W. P. Hay‡, Eliot H. Ohlstein‡, Derk J. Bergsma* & Stephen A. Douglas‡**

*Departments of * Molecular Biology, ‡ Pulmonary and Cardiovascular Pharmacology, § Functional Gene Analysis, ‖ Pathology, ¶ Laboratory Animal Sciences, # Immunology, ☆ Protein Biochemistry and ** Gene Expression Sciences, Smith Kline Beecham Pharmaceuticals, 709 Swedeland Road, King of Prussia, Pennsylvania 19406-0939, USA and Southern Way, Harlow, Essex CM19 5AW, UK*

† *These authors contributed equally to this work*

Urotensin-II (U-II) is a vasoactive 'somatostatin-like' cyclic peptide which was originally isolated from fish spinal cords[1,2], and which has recently been cloned from man[3]. Here we describe the identification of an orphan human G-protein-coupled receptor homologous to rat GPR14 (refs 4, 5) and expressed predominantly in cardiovascular tissue, which functions as a U-II receptor. Goby and human U-II bind to recombinant human GPR14 with high affinity, and the binding is functionally coupled to calcium mobilization. Human U-II is found within both vascular and cardiac tissue (including coronary atheroma) and effectively constricts isolated arteries from non-human primates. The potency of vasoconstriction of U-II is an order of magnitude greater than that of endothelin-1, making human U-II the most potent mammalian vasoconstrictor

© 1999 Macmillan Magazines Ltd

identified so far. *In vivo*, human U-II markedly increases total peripheral resistance in anaesthetized non-human primates, a response associated with profound cardiac contractile dysfunction. Furthermore, as U-II immunoreactivity is also found within central nervous system and endocrine tissues, it may have additional activities.

In an effort to identify novel G-protein-coupled receptors (GPCRs), we probed a human genomic library with rat GPR14 (SENR)[4,5], an orphan GPCR similar to somatostatin receptors. We isolated a 9-kilobase (kb) genomic clone which encoded a 389-residue human GPCR (75% identity to rat GPR14; Fig. 1). GPR14 messenger RNA was most abundant in the heart and pancreas (no expression was detected in 15 discrete brain regions; see Supplementary Information); however, using quantitative polymerase chain reaction with reverse transcription (RT-PCR), low levels of transcript were detectable in thalamus, superior occipital gyrus and substantia nigra. Additional RT-PCR revealed expression in human cardiac (atria and ventricle) and arterial (aorta) tissue, endothelial (coronary artery and umbilical vein) cells and smooth muscle (coronary artery and aortic) cell lines, but not in vena cava nor in a venous (renal vein) smooth muscle cell line.

Human GPR14 was subcloned into a mammalian expression vector and transfected into HEK-293 cells. In a 'reverse pharmacological approach'[6,7], the cells were used to search for a ligand activating GPR14 using a calcium-mobilization assay. Using a fluorescent imaging plate reader (FLIPR), transiently transfected cells were exposed to over 700 known and putative GPCR agonists. We detected a robust calcium-mobilization response in cells transfected with either rat or human GPR14 only upon challenge with goby U-II (effector concentration for half maximum response (EC_{50}) of 0.78 ± 0.18 and 0.47 ± 0.14 nM, respectively; Fig. 2a). This response was highly selective for goby U-II and was not induced by any of the other ligands we tested. Cells transfected with expression vector alone, or vectors encoding other orphan GPCRs such as GPR7 or GPR8, which are also homologous to the somatostatin receptors[8], did not respond to goby U-II.

A human GPCR that selectively responded to a non-mammalian neuropeptide indicated the possible existence of a human orthologue. A search of GenBank using the carp U-II sequence[9] yielded a match to a human expressed sequence tag (EST) with 25% identity to the fish sequence. Using this EST, we isolated a 688-base pair (bp) complementary DNA encoding human U-II (Fig. 3). The deduced propeptide sequence contained an amino-terminal signal sequence (cleaved at residue 17) and three putative polybasic proteolytic cleavage sites (Fig. 3), but varied at the amino terminus from the human U-II propeptide described subsequently in ref. 3, probably as a result of alternative splicing. The mature sequence (ETPDCFWKYCV) was identical to human U-II (ref. 3), and it retained the cyclic hexapeptide sequence (CFWKYC) that is absolutely conserved across species[1,2]. Expression of the U-II transcript was restricted to the spinal cord and medulla oblongata (see Supplementary Information), consistent with previous reports in fish, frogs and humans[1–3].

Human U-II induced concentration-dependent increases in intracellular calcium in a HEK-293 cell line expressing human GPR14 (EC_{50} = 0.62 ± 0.17 nM, n = 6; Fig. 2b). ^{125}I-labelled goby U-II bound saturably and with high affinity to membranes prepared from these cells (Fig. 2c; K_d = 0.43 ± 0.01 nM; B_{max} = 447 ± 58 fmol mg^{-1} protein; n = 3). Goby and human U-II displaced the radioligand with comparable affinities

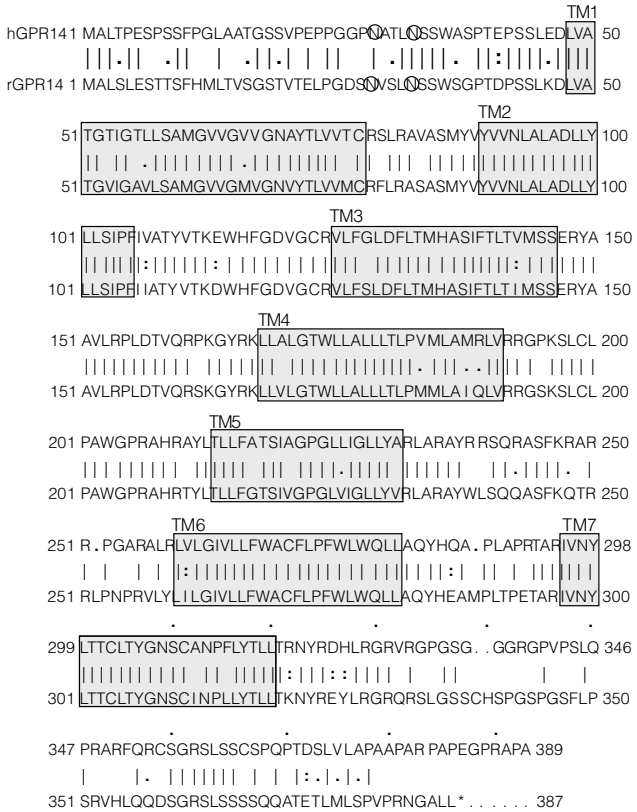

Figure 1 Alignment of rat (r) and human (h) GPR14 polypeptide sequences. The predicted seven transmembrane (TM) spanning regions are shaded and potential N-linked glycosylation sites are circles. GenBank accession number of human GPR14 is AF140631.

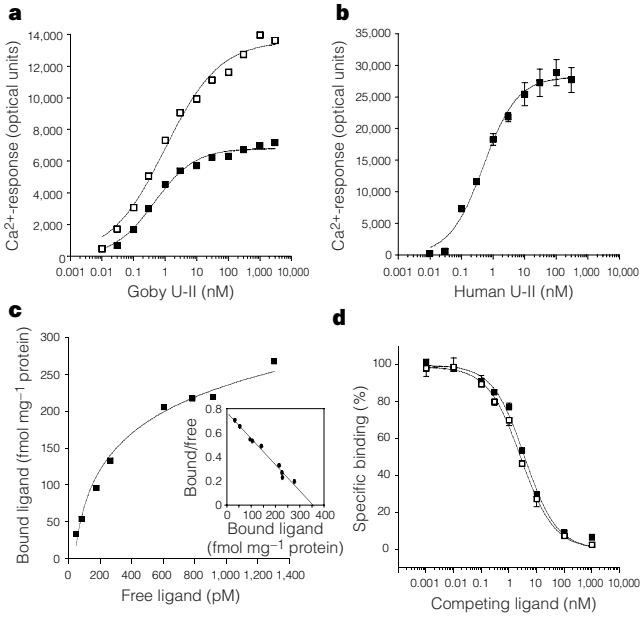

Figure 2 GPR14 is a U-II receptor. **a**, Goby U-II-induced Ca^{2+}-mobilization (FLIPR) in HEK-293 cells transiently transfected with rat (filled squares) or human GPR14 (open squares). **b**, Ca^{2+}-mobilization response to human U-II in clonal HEK-293 cell lines stably transfected with human GPR14. **c**, Saturation binding isotherm for ^{125}I-labelled goby U-II in cell membranes from HEK-293 cells stably transfected with human GPR14 (inset, Scatchard analysis). **d**, Competition binding curves for human (filled squares) and goby U-II (open squares) with human GPR14.

© 1999 Macmillan Magazines Ltd

```
  1  TGCCGGTGCCTTCATGGGCAGGACTAGGCCGAAAACTCCCCAGATTGTCATTCTTCAGGG   60
 61  ATGGCAGCCCTAAACACAGCATGGCAACTCATCTACTCACTCATGAAAGATTAAAAAATG   120
                                                          M
121  GAAACCAACGTATTTCATCTTATGCTCTGCGTCACTTCTGCTCGGACTCATAAATCCACG   180
     E  T  N  V  F  H  L  M  L  C  V  T  S  A  R  T  H  K  S  T
181  TCTCTTTGCTTTGGCCACTTCAACTCATATCCAAGCCTTCCTTTAATTCATGATTTATTG   240
     S  L  C  F  G  H  F  N  S  Y  P  S  L  P  L  I  H  D  L  L
241  CTGGAAATATCCTTTCAACTCTCAGCACCTCATGAAGACGCGCGCTTAACTCCGGAGGAG   300
     L  E  I  S  F  Q  L  S  A  P  H  E  D  A  R  L  T  P  E  E
301  CTAGAAAGAGCTTCCCTTCTACAGATACTGCCAGAGATGCTGGGTGCAGAAAGAGGGGAT   360
     L  E  R  A  S  L  L  Q  I  L  P  E  M  L  G  A  E  R  G  D
361  ATTCTCAGGAAAGCAGACTCAAGTACCAACATTTTTAACCCAAGAGGAAATTTGAGAAAG   420
     I  L  R  K  A  D  S  S  T  N  I  F  N  P  R  G  N  L  R  K
421  TTTCAGGATTTCTCTGGACAAGATCCTAACATTTTACTGAGTCATCTTTTGGCCAGAATC   480
     F  Q  D  F  S  G  Q  D  P  N  I  L  L  S  H  L  L  A  R  I
481  TGGAAACCATACAAGAAACGTGAGACTCCTGATTGCTTCTGGAAATACTGTGTCTGAAGT   540
     W  K  P  Y  K  K  R  E  T  P  D  C  F  W  K  Y  C  V
541  GAAATAAGCATCTGTTAGTCAGCTCAGAAACACCCATCTTAGAATATGAAAAATAACACA   600
601  ATGCTTGATTTGAAAACAGTGTGGAGAAAAACTAGGCAAACTACACCCTGTTCATTGTTA   660
661  CCTGGAAAATAAATCCTCTATGTTTTGC  688
```

Figure 3 Nucleotide and deduced peptide sequence of human U-II propeptide cDNA. Putative polybasic cleavage sites are shown in bold and underlined. The putative mature human U-II is shown in italics. GenBank accession number is AF140630.

Table 1 Relative contractile potency of human U-II in non-human primates

Vessel	Human urotensin-II $-\log[EC_{50}]$	Endothelin-1 $-\log[EC_{50}]$	Relative potency
Arterial tissue			
Left anterior descending coronary	9.39 ± 0.40	8.20 ± 0.32*	15
Left circumflex coronary	9.56 ± 0.05	n.d.	
Mesenteric	9.35 ± 0.26	8.24 ± 0.28*	13
Pulmonary	9.29 ± 0.16	7.84 ± 0.06***	28
Renal	9.59 ± 0.36	8.83 ± 0.24	6
Proximal descending thoracic aorta	8.96 ± 0.24	n.d.	
Distal descending thoracic aorta	9.06 ± 0.22	n.d.	
Distal abdominal aorta	9.37 ± 0.13	n.d.	
Basilar	10.00 ± 0.16	n.d.	
Common carotid	9.16 ± 0.08	n.d.	
Internal mammary	9.30 ± 0.08	n.d.	
Venous tissue			
Portal vein	<7.00	7.00 ± 0.77	
Jugular vein	<7.00	8.88 ± 0.21	

All values are mean ± s.e.m. (n = 3–4). Statistical comparisons made by analysis of variance (post-hoc Fisher's least-squares difference): *$P < 0.05$ and ***$P < 0.001$. n.d., not determined.

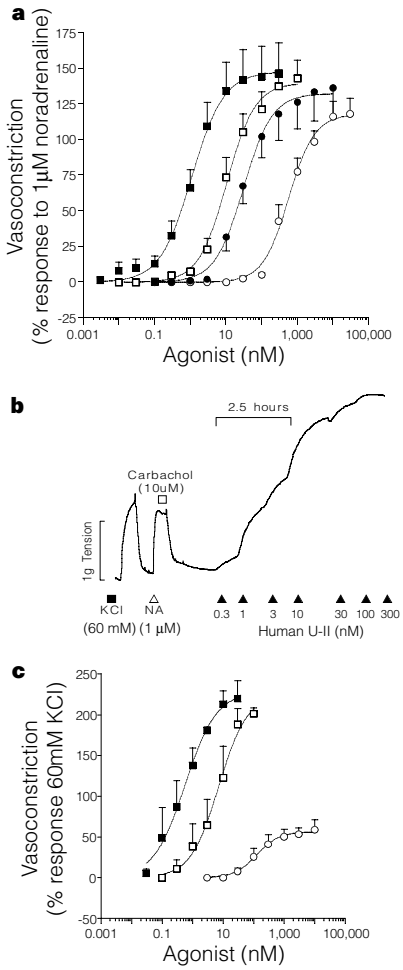

Figure 4 Human U-II is a potent vasoconstrictor. **a**, Concentration-dependent contraction of rat isolated aorta by human U-II (filled squares; $n = 13$), ET-1 (open squares; $n = 11$), noradrenaline (filed circles; $n = 13$) and serotonin (open circles; $n = 4$). **b**, Trace showing concentration-dependent contraction of the primate isolated aorta by human U-II (filled triangles). Responses to standard concentrations of KCl (filled square) and noradrenaline (open triangle) are shown (successful endothelial denudation is shown by the lack of carbachol-induced vasodilation; open square). **c**, Concentration-dependent contraction of the cynomolgus monkey isolated coronary artery ($n = 4$) in response to human U-II (filled squares), ET-1 (open squares) and serotonin (open circles).

($K_i = 2.06 \pm 0.29$ and 1.99 ± 0.23 nM, respectively; Fig. 2d). Hill coefficients for goby and human U-II approximated to unity ($n_H = 0.8 \pm 0.1$ and 0.9 ± 0.1, respectively), indicative of interactions with a single, homogeneous population of binding sites. Binding sites for fish U-II are found in rat arterial membranes, although receptor density is extremely low (2–20 fmol mg^{-1} protein[10]). We have made similar observations in rat cardiac membranes ($K_d = 0.35$ nM; $B_{max} = 3.8$ fmol mg^{-1} protein). Although U-II and somatostatin are structurally similar[11], human GPR14 functioned as a U-II-selective receptor: 1 μM concentrations of somatostatin$_{(1–14)}$, urotensin-I, vasopressin, angiotensin-II, MCH, salmon calcitonin and NPY did not compete for binding; neither did they stimulate calcium mobilization in HEK-293 cells expressing human GPR14.

Immunohistochemical evaluation of monkey and human tissue showed (see Supplementary Information) that the vasculature contained U-II-like immunoreactivity. Diffuse immunostaining was observed in human cardiomyocytes and coronary atherosclerotic plaque, where the staining was intense within the lipid-laden smooth muscle/macrophage-rich regions. We noted additional immunoreactivity within spinal cord ventral horn motor neurons and acinar cells lining the thyroid follicles.

Human and goby U-II induced potent and efficacious contractions in the isolated thoracic aorta of rat ($-\log[EC_{50}] = 9.09 \pm 0.19$, $n = 13$; $-\log[EC_{50}] = 9.22 \pm 0.18$, $n = 15$, respectively; Fig. 4a). Human U-II was significantly more potent ($P < 0.001$) than endothelin-1 (ET-1), noradrenaline and serotonin ($-\log[EC_{50}] = 7.90 \pm 0.11$, 7.58 ± 0.11 and 6.27 ± 0.12, respectively; $n = 11$, 13 and 4, respectively; Fig. 4a). Thus, U-II is the most potent human vasoconstrictor peptide identified so far (16-fold more potent than ET-1 in rat).

The vasoconstrictor activity of human U-II was limited to the thoracic aorta in rat: abdominal aorta or femoral and renal arteries did not contract (radioligand binding sites were undetectable in vessels distal to the aortic arch)[10]. Consequently, U-II lacks systemic pressor activity in anaesthetized rats upon intravenous (i.v.) administration[12,13]. In contrast, however, human U-II caused contraction in all non-human primate arterial vessels studied, including both elastic and muscular arteries (Fig. 4b, c). EC_{50} values were subnanomolar, making human U-II 6–28-fold more potent than ET-1 (Table 1). Unlike ET-1, however, the contractile actions were restricted to the arterial side of the vasculature, consistent with the differential expression of human GPR14 determined by PCR. Thus, the contractile profile of U-II is species-dependent and U-II exhibits an 'anatomically diverse' contractile profile in the arterial vasculature of the primate.

Following this striking *in vitro* profile, we carried out haemodynamic evaluation in anaesthetized monkeys. Systemic administra-

© 1999 Macmillan Magazines Ltd

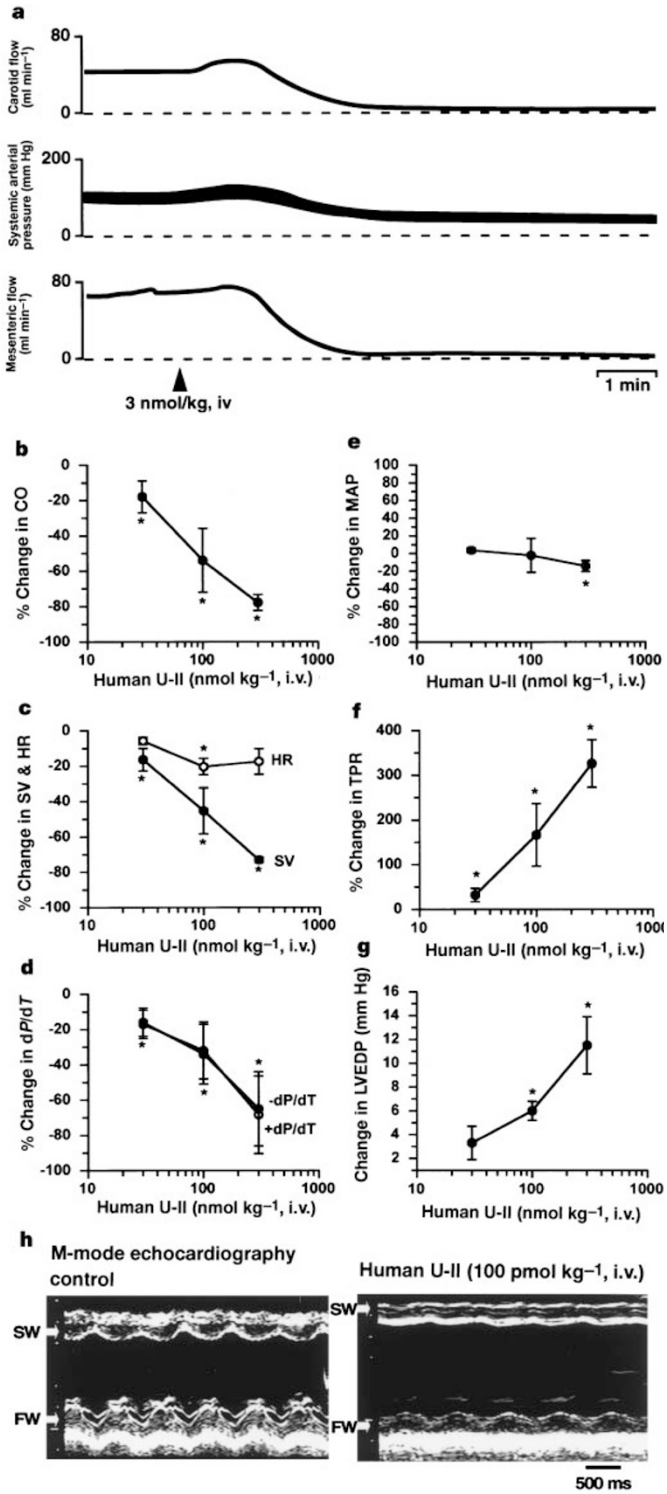

Figure 5 Human U-II produces cardiovascular dysfunction in the anaesthetized monkey. **a**, Fatal circulatory collapse (precipitous falls in systemic pressure and regional flows) induced by bolus i.v. human U-II. Alterations in cardiac output (CO) (**b**), heart rate (HR, open circles) and stroke volume (SV, filled circles) (**c**), myocardial contractility (d*P*/d*t*) (**d**), mean arterial pressure (MAP) (**e**), total peripheral resistance (TPR) (**f**) and left ventricular end diastolic pressure (LVEDP) (**g**). *, $P < 0.05$ relative to vehicle ($n = 5$). **h**, M-mode echocardiographic images of the left ventricle before and 7 min after 100 pmol kg^{-1}, i.v. human U-II show severe attenuation of septal (SW) and free wall (FW) motion.

tion of human U-II elicited a complex dose-dependent haemodynamic resonse that culminated in severe myocardial depression and fatal circulatory collapse (Fig. 5a). Unusually, a 300 pmol kg^{-1} dose of U-II, which induces a 300% increase in total peripheral resistance (indicative of systemic vasoconstriction), did not cause concomitant systemic hypertension. The ability of U-II to induce marked systemic vasoconstriction while also causing catastrophic myocardial contractile dysfunction (for example, 80% decrease in d*P*/d*t* and stroke volume) differentiates it from other peptides such as ET-1 and angiotensin-II. For example, 1 nmol kg^{-1} ET-1 i.v. (sufficient to elevate total peripheral resistance) is accompanied, not by cardiovascular collapse and systemic hypotension, but rather by a sustained (≤1 h) 60 mm Hg increase in arterial pressure[14].

The primate responses were clearly different from those reported in rats[12,13]. At doses <30 pmol kg^{-1} i.v., human U-II slightly increased cardiac output and reduced regional vascular resistance, with little or no change in arterial blood pressure. In contrast, at doses ≥30 pmol kg^{-1}, human U-II decreased myocardial function and increased vascular resistance. Haemodynamic and echocardiographic analysis demonstrated a dose-dependent reduction in cardiac output (Fig. 5b), the result of mild bradycardia and severely attenuated stroke volume (Fig. 5c). Myocardial contractility was severely depressed, as seen by reductions in d*P*/d*t* (Fig. 5d). Despite a marked decrease in cardiac output, sub-lethal doses reduced mean arterial pressure only moderately (Fig. 5e) because of a threefold increase in total peripheral resistance (Fig. 5f). Decreases in regional blood flows and a dose-dependent increase in left ventricular end diastolic pressure (Fig. 5g) indicated systemic vasoconstriction. The severe loss of myocardial contractility was shown by M-mode echocardiography (Fig. 5h) in which grossly attenuated septal and free-wall motion was evident (ultimately, this effect was terminal at doses ranging from 100–3,000 pmol kg^{-1}). Systemic human U-II administration produced ST segment changes in the electrocardiogram typical of those seen during myocardial ischaemia.

In summary, we have isolated a human GPCR that exhibits the pharmacological characteristics of a U-II receptor. Cells expressing this receptor exhibit high-affinity binding sites for, and respond to, both goby and human U-II. Furthermore, we have demonstrated that U-II is the most potent vasoconstrictor identified so far. Systemic administration is associated with profound cardiovascular collapse. As human U-II-like immunoreactivity is found within cardiac and vascular tissue (including coronary atheroma), this peptide may influence cardiovascular homeostasis and pathology (for example, in ischaemic heart disease and congestive heart failure). Finally, the detection of immunoreactivity within spinal cord and thyroid tissue raises the possibility that U-II may also influence central nervous system and endocrine function in man. □

Methods

Cloning

A human genomic placental library (Stratagene) was screened with a ^{32}P-labelled 1.2-kb PCR-derived clone encoding rat GPR14 (ref. 4), and we identified a positive phage plaque. Two kilobases of insert was sequenced and determined to be homologous to rat GPR14. Human GPR14 was isolated by PCR and subcloned into pCDN (ref. 15). HEK-293 cells were transiently or stably transfected using Lipofectamine Plus (Life Technologies). Using the published fish cDNA sequence[9], a search of the GenEMBL EST database identified a human cDNA (AA535545) encoding a putative U-II orthologue. After, 5′-rapid amplification of cDNA ends (RACE) (placenta and Raji Marathon Ready cDNAs; Clontech), we sequenced and subcloned the resultant products into pCR2.1 (Invitrogen).

Peptide synthesis

Human U-II peptidyl resin was synthesized (Milipore/Biosearch 9600 synthesizer), cleaved and de-protected before purification by reverse-phase HPLC[16]. All other peptides were from Bachem.

© 1999 Macmillan Magazines Ltd

Calcium mobilization

We used a microtitre-plate-based calcium-mobilization FLIPR assay, as described previously[17], for the functional identification of ligands that activate HEK-293 cells expressing recombinant GPR14. Ligands we tested included micromolar concentrations of all known mammalian neuropeptides and ≥10 μM concentrations of all known steroid, lipid and amine transmitters.

Radioligand binding

Membranes from HEK-293 cells stably transfected with human GPR14 were pre-coupled to wheatgerm-agglutinin-coated SPA beads (Amersham). Using mono-iodinated goby U-II (^{125}I-labelled Tyr^{10}, chloramine T, 2000 Ci mmol^{-1}; 5 mM $MgCl_2$, 0.1% BSA, 20 mM Tris-HCl pH 7.4, 25 μg protein; 25 °C), equilibrium binding was measured in 96-well plates (Wallac) after 45 min[18]. Non-specific binding, determined using 1 μM unlabelled U-II, was ~10% of total binding. There was no specific binding to mock-transfected HEK-293 membranes. We determined protein using biochonic acid (Pierce). Kinetic analysis was by nonlinear least square fitting (GraphPad).

Isolated blood vessel studies

Isolated arterial rings from male Sprague–Dawley rats (400 g) and cynomolgus monkeys (*Macaca fascicularis*) (5 kg) were suspended in organ baths containing Krebs (37 °C; 95% O_2; 5% CO_2)[19]. Changes in isometric force were recorded under optimal resting tension. Cumulative agonist concentration–response curves were normalized to 60 mM KCl or 1 μM noradrenaline and fitted to a logistic equation[19]. Unless stated otherwise, responses were measured in the presence of 10 μM indomethacin using vessels denuded by rubbing (confirmed as a loss of dilator response to 10 μM carbachol).

Haemodynamics and echocardiography

All procedures were performed in accordance with the Guide for the Care and Use of Laboratory Animals (DHSS publication NIH 85-23). Adult male cynomolgus monkeys (5–7 kg) were treated with atropine sulphate (25 μg kg^{-1} subcutaneous) and anaesthetized with ketamine (10 mg kg^{-1} intramuscular). After endotracheal intubation, anaesthesia was maintained with 1–3% isoflurane. We prepared the animals for monitoring of systemic haemodynamics. Echocardiography (Doppler, M-mode and 2-D, ATL5000) was carried out at 2–3 min intervals. Vehicle administration (0.9% NaCl) was followed by the cumulative administration of human U-II.

Statistics

Values are expressed as mean ± s.e.m. n is the number of individual observations made in a particular group. Statistical comparisons were made by one-way analysis of variance (Fisher's protected least-squares difference) and differences considered significant where $P < 0.05$.

Received 8 July; accepted 13 August 1999.

1. Bern, H. A., Pearson, D., Larson, B. A. & Nishioka, R. S. Neurohormones from fish tails: the caudal neurosecretory system. I. "Urophysiology" and the caudal neurosecretory system of fishes. *Recent Prog. Horm. Res.* **41,** 533–552 (1985).
2. Conlon, J. M., Yano, K., Waugh, D. & Hazon, N. Distribution and molecular forms of urotensin II and its role in cardiovascular regulation in vertebrates. *J. Exp. Zool.* **275,** 226–238 (1996).
3. Coulouarn, Y. *et al.* Cloning of the cDNA encoding the urotensin II precursor in frog and human reveals intense expression of the urotensin II gene in motoneurons of the spinal cord. *Proc. Natl Acad. Sci. USA* **95,** 15803–15808 (1998).
4. Marchese, A. *et al.* Cloning and chromosomal mapping of three novel genes, GPR9, GPR10, and GPR14, encoding receptors related to interleukin 8, neuropeptide Y, and somatostatin receptors. *Genomics* **29,** 335–344 (1995).
5. Tal, M. *et al.* A novel putative neuropeptide receptor expressed in neural tissue, including sensory epithelia. *Biochem. Biophys. Res. Commun.* **209,** 752–759 (1995).
6. Stadel, J. M., Wilson, S. & Bergsma, D. J. Orphan G protein-coupled receptors: a neglected opportunity for pioneer drug discovery. *Trends Pharmacol. Sci.* **18,** 430–437 (1997).
7. Libert, F., Vassart, G. & Parmentier, M. Current developments in G-protein-coupled receptors. *Curr. Opin. Cell Biol.* **3,** 218–223 (1991).
8. O'Dowd, B. F. *et al.* The cloning and chromosomal mapping of two novel human opioid-somatostatin-like receptor genes, GPR7 and GPR8, expressed in discrete areas of the brain. *Genomics* **28,** 84–91 (1995).
9. Ohsako, S., Ishida, I., Ichikawa, T. & Deguchi, T. Cloning and sequence analysis of cDNAs encoding precursors of urotensin II-alpha and -gamma. *J. Neurosci.* **6,** 2730–2735 (1986).
10. Itoh, H., McMaster, D. & Lederis, K. Functional receptors for fish neuropeptide urotensin II in major rat arteries. *Eur. J. Pharmacol.* **149,** 61–66 (1988).
11. Pearson, D. *et al.* Urotensin II: a somatostatin-like peptide in the caudal neurosecretory system of fishes. *Proc. Natl Acad. Sci. USA* **77,** 5021–5024 (1980).
12. Gibson, A., Wallace, P. & Bern, H. A. Cardiovascular effects of urotensin II in anesthetized and pithed rats. *Gen. Comp. Endocrinol.* **64,** 435–439 (1986).
13. Hasegawa, J., Kobayashi, Y. & Kobayashi, H. Vasodepressor effects of urotensin II in rats. *Neuroendocrinol. Lett.* **14,** 357–363 (1992).
14. Yanagisawa, M. *et al.* A novel potent vasoconstrictor peptide produced by vascular endothelial cells. *Nature* **332,** 411–415 (1988).
15. Aiyar, N. *et al.* Human AT1 receptor is a single copy gene: characterization in a stable cell line. *Mol. Cell Biochem.* **131,** 75–86 (1994).
16. King, D. S., Fields, C. G. & Fields, G. B. A cleavage method which minimizes side reactions following Fmoc solid phase peptide synthesis. *Int. J. Pept. Protein Res.* **36,** 255–266 (1990).
17. Chambers, J. *et al.* Melanin-concentrating hormone is the cognate ligand for the orphan G-protein-coupled receptor SLC-1. *Nature* **400,** 261–265 (1999).
18. Elshourbagy, N. A. *et al.* Molecular cloning and characterization of the porcine calcitonin gene-related peptide receptor. *Endocrinology* **139,** 1678–1683 (1998).
19. Douglas, S. A. & Hiley, C. R. Endothelium-dependent mesenteric vasorelaxant effects and systemic actions of endothelin (16–21) and other endothelin-related peptides in the rat. *Br. J. Pharmacol.* **104,** 311–320 (1991).

Supplementary Information is available on *Nature*'s World-Wide Web site (http://www.nature.com) or as paper copy from the London editorial office of *Nature*.

Acknowledgements

We dedicate this Letter to the memory of our friend and colleague, the late J. M. Stadel. We thank D. Ashton, P. Buckley, T. Covatta, J. Culp, G. Dytko, L. Floyd, P. Hieble, M. Luttmann, G. McCafferty, D. Naselsky, P. Nuthulaganti, P. Ryan and A. Sulpizio for their assistance and comments during the preparation of this manuscript. We thank B. O'Dowd, University of Toronto for the rat GPR14 cDNA clone.

Correspondence and requests for materials should be addressed to R.S.A. (e-mail: bob_ames-1@sbphrd.com). The GenBank accession numbers for human GPR14 and U-II are AF140631 and AF140630, respectively.

A kinase-regulated PDZ-domain interaction controls endocytic sorting of the β2-adrenergic receptor

Tracy T. Cao*, Heather W. Deacon*, David Reczek†, Anthony Bretscher† & Mark von Zastrow‡

* *Department of Biochemistry and Biophysics, University of California, San Francisco, San Francisco, California 94143 USA*
† *Section of Biochemistry, Molecular and Cell Biology, Cornell University, Ithaca, New York 14853, USA*
‡ *Program in Cell Biology, Cellular and Molecular Pharmacology and Psychiatry, University of California, San Francisco, San Francisco, California 94143, USA*

A fundamental question in cell biology is how membrane proteins are sorted in the endocytic pathway. The sorting of internalized β2-adrenergic receptors between recycling endosomes and lysosomes is responsible for opposite effects on signal transduction and is regulated by physiological stimuli[1,2]. Here we describe a mechanism that controls this sorting operation, which is mediated by a family of conserved protein-interaction modules called PDZ domains[3]. The phosphoprotein EBP50 (for ezrin–radixin–moesin(ERM)-binding phosphoprotein-50)[4] binds to the cytoplasmic tail of the β2-adrenergic receptor through a PDZ domain and to the cortical actin cytoskeleton through an ERM-binding domain. Disrupting the interaction of EBP50 with either domain or depolymerization of the actin cytoskeleton itself causes missorting of endocytosed β2-adrenergic receptors but does not affect the recycling of transferrin receptors. A serine residue at position 411 in the tail of the β2-adrenergic receptor is a substrate for phosphorylation by GRK-5 (for G-protein-coupled-receptor kinase-5) (ref. 5) and is required for interaction with EBP50 and for proper recycling of the receptor. Our results identify a new role for PDZ-domain-mediated protein interactions and for the actin cytoskeleton in endocytic sorting, and suggest a mechanism by which GRK-mediated phosphorylation could regulate membrane trafficking of G-protein-coupled receptors after endocytosis.

© 1999 Macmillan Magazines Ltd